Graduate School ETD Form 9
(Revised 12/07)

PURDUE UNIVERSITY
GRADUATE SCHOOL
Thesis/Dissertation Acceptance

This is to certify that the thesis/dissertation prepared

By CHEOL WOONG LIM

Entitled
MATHEMATICAL ANALYSIS OF THE LITHIUM ION TRANSPORT IN LITHIUM ION BATTERIES USING THREE DIMENSIONAL RECONSTRUCTED ELECTRODES.

For the degree of Master of Science in Mechanical Engineering

Is approved by the final examining committee:

Likun Zhu
Chair

Jian Xie

Youngsik Kim

To the best of my knowledge and as understood by the student in the *Research Integrity and Copyright Disclaimer (Graduate School Form 20)*, this thesis/dissertation adheres to the provisions of Purdue University's "Policy on Integrity in Research" and the use of copyrighted material.

Approved by Major Professor(s): Likun Zhu

Approved by: Sohel Anwar 04/20/2012
Head of the Graduate Program Date

Graduate School Form 20
(Revised 9/10)

PURDUE UNIVERSITY
GRADUATE SCHOOL

Research Integrity and Copyright Disclaimer

Title of Thesis/Dissertation:

MATHEMATICAL ANALYSIS OF THE LITHIUM ION TRANSPORT IN LITHIUM ION BATTERIES USING THREE DIMENSIONAL RECONSTRUCTED ELECTRODES.

For the degree of Master of Science in Mechanical Engineering

I certify that in the preparation of this thesis, I have observed the provisions of *Purdue University Executive Memorandum No. C-22,* September 6, 1991, *Policy on Integrity in Research.**

Further, I certify that this work is free of plagiarism and all materials appearing in this thesis/dissertation have been properly quoted and attributed.

I certify that all copyrighted material incorporated into this thesis/dissertation is in compliance with the United States' copyright law and that I have received written permission from the copyright owners for my use of their work, which is beyond the scope of the law. I agree to indemnify and save harmless Purdue University from any and all claims that may be asserted or that may arise from any copyright violation.

CHEOL WOONG LIM

Printed Name and Signature of Candidate

04/20/2012

Date (month/day/year)

*Located at http://www.purdue.edu/policies/pages/teach_res_outreach/c_22.html

MATHEMATICAL ANALYSIS OF THE LITHIUM ION TRANSPORT IN LITHIUM ION BATTERIES USING THREE DIMENSIONAL RECONSTRUCTED ELECTRODES

A Thesis
Submitted to the Faculty
of
Purdue University
by
Cheol Woong Lim

In Partial Fulfillment of the
Requirements for the Degree
of
Master of Science in Mechanical Engineering

May 2012
Purdue University
Indianapolis, Indiana

ACKNOWLEDGMENTS

I would like to gratefully acknowledge my advisor, Dr. Likun Zhu, for his supervision, guidance, and scientific support during the entire course of this research and thesis work. Dr. Zhu generously shared with me his research experience and academic approaches.

I would also like to appreciate my advisory committee members, Dr. Jian Xie and Dr. Youngsik Kim for their time and insight during the completion of my thesis. Dr. Xie encouraged me to study renewable energy area and elucidated concepts of electrochemistry in his class. Dr. Kim always guided me in right directions.

I would like to expand my special thanks to my collaborators from Dr. Yan Bo, Dr. Hui He, Dr. Yadong Liu, and Mahootcheian Asl, Nina for their fruitful discussions and valuable contributions that led to successful completion of the research.

Finally, I would like to dedicate this manuscript to my wife and family. Without her love and affections I would not have made this far.

TABLE OF CONTENTS

Page

LIST OF TABLES

LIST OF FIGURES

Figure Page

Figure Page

ABSTRACT

Lim, Cheol Woong. M.S.M.E., Purdue University, May 2012. Mathematical Analysis of the Lithium Ion Transport in Lithium Ion Batteries Using Three Dimensional Reconstructed Electrodes. Major Professor: Likun Zhu.

Computational analysis of lithium ion batteries has been improved since Newman and et al. suggested the porous electrode theory. It assumed the electrode as a simple structure of homogeneous spherical particles. Bruggeman relationship which characterizes porous material by a simple equation was adopted in the homogeneous electrode model instead of the electrode morphology. To improve the prediction of a cell performance, the numerical analysis requires the realistic microstructure of the cell.

Based on the experimentally determined microstructure of the positive and negative electrodes of a lithium ion battery (LIB) using x-ray micro/nano-CT technology, three dimensional (3D) simulations have been presented in this research. Tortuosity of the microstructures has been calculated by a linear diffusion equation to characterize the 3D morphology. The obtained tortuosity and porosity results pointed out that the Bruggeman relationship is not sufficiently estimate the tortuosity by the porosity of electrodes.

We studied the diffusion-induced stress numerically based on realistic morphology of reconstructed particles during the lithium ion intercalation process. Diffusion-induced stresses were simulated at different C rates under galvonostatic conditions and compared with spherical particles. The simulation results showed that the intercalation stresses of particles depend on their geometric characteristics. The highest

von Mises stress and tresca stress in a real particle are several times higher than the stresses in a spherical particle with the same volume.

With the reconstructed positive electrode structure, local effects in the LIB cathode electrode during galvanostatic discharge process have been studied. The simulation results reported that large current density usually occurs at the joints between cathode active material particles and in the small channels in electrolyte, which will generate high electric joule power. By using the 3D real image of a LIB cathode electrode, numerical simulation results revealed that the spatial distribution of variable fields such as concentration, voltage, reaction rate, overpotential, and etc. in the cathode electrode are complicated and non-uniform, especially at high discharge rates.

1. INTRODUCTION

1.1. Lithium Ion Battery

In recent decades, renewable energy sources that come from natural resources such as wind, sunlight, rain, and tides have developed to reduce the consumption of fossil fuel which can cause global warming. The clean energy which is generated by wind power, hydropower, solar energy, and biofuel requires a suitable energy storage system for portable applications. One of the most available candidates for energy storage systems are rechargeable lithium ion batteries (LIBs). Moreover, LIBs have attracted lots of interest in automobile applications. Those applications require high energy and power sources.

The increasing demand for power sources with high energy and power densities has generated a worldwide effort towards the development of new active materials and fabrication methods for LIBs. Those efforts lead the performance improvements of the LIBs since the first LIB released by Sony Corporation in 1991. However, the technology has not reached the market demands in terms of lifetime and durability of the cell. For example, the United State Advanced Battery Council sets a target performance that requires 10 years lifetime at 80% of depth of charge up to 1000 cycles, which has not been achieved yet.

The reminder of this chapter provides an introduction to LIB technology, the degradation mechanism of electrode components, and literature reviews of various mathematical models used in this thesis. The chapter concludes with an overview and motivations of the research.

1.1.1. Anatomy of a Lithium Ion Battery

A schematic diagram of LIBs shows in Figure 1.1. LIBs typically consist of a graphite negative electrode (anode) on a copper current collector, a lithium metal oxide positive electrode (cathode) on an aluminum foil current collector, micro-porous separator between the electrodes, a liquid electrolyte that consists of a lithium salt dissolved in an organic solvent, and an external circuit which connects the two current correctors.

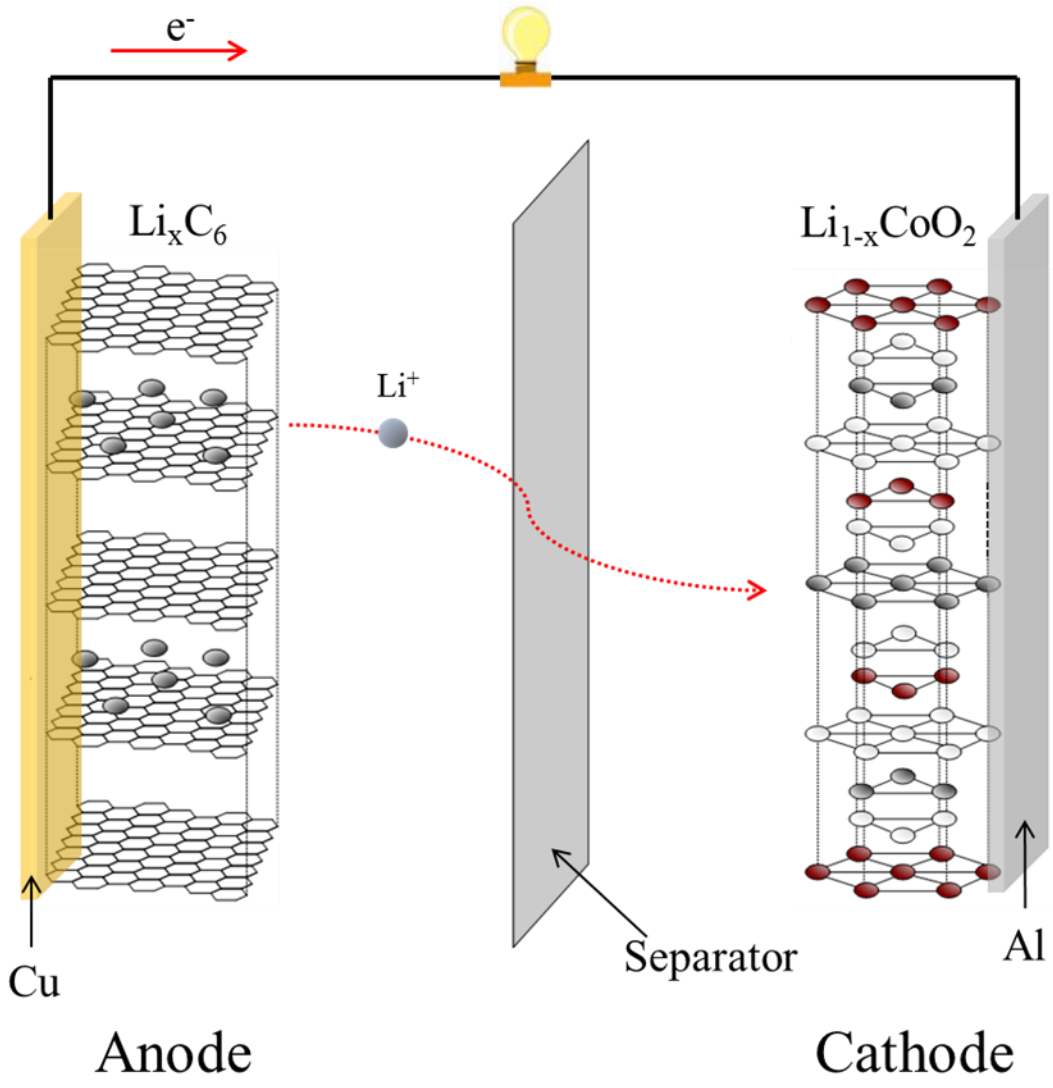

Figure 1.1 Schematic description of a lithium-ion cell based on electrochemical intercalation process (discharge)

In this research, we adopt graphite (LiC_6) as a negative active material and lithium cobalt oxide ($LiCoO_2$) as a positive active material. A lithium ion insertion or extraction reaction in the negative electrode is described by a charge-transfer reaction of the form

$$Li_xC_6 \rightleftharpoons xLi^+ + xe^- + 6C$$

For the positive electrode, the half reaction is

$$Li_{1-x}CoO_2 + xLi^+ + xe^- \rightleftharpoons LiCoO_2$$

A fully charged cell starts to discharge by the voltage difference of the two electrodes when the external circuit is closed. At the anode site, lithium ions and electrons are produced by an oxidation reaction. The produced lithium ions and electrons are reached in the cathode site through different paths. The lithium ions, which are only allowed to penetrate the separator, migrate to the cathode site through the salt electrolyte. At the same time, conducted electrons on copper foil current corrector flow through the external circuit to cathode site. The transported lithium ions and electrons are reacted with the cathode material. The reverse reactions occur during charging process.

1.1.2. Anode Active Material

Graphite is one of a preferred anode material in LIBs and thus the material has been studied to improve the performance in many research groups. The capacity and power fade are caused by various reasons such as electrolyte decomposition, structural changes, gas generation, corrosion, and etc [1].

Graphite, as an anode active material, operates at outside voltages of the electrochemical window of electrolyte components. The electrochemical instability causes irreversible consumption of lithium ions on the electrode surface where is surrounded by electrolyte. This unavoidable electrolyte decomposition occurs mainly at the first few cycles and the decomposition product layer is called as a solid electrolyte interphase (SEI) layer [2]. The SEI layers are considered as permeable sites where

lithium ions can intercalate/deintercalate into/from the negative active material but protect other electrolyte components and electrons. The formation of SEI layers causes loss of lithium ions (capacity loss) that is dependent on the specific surface area of the graphite as well as the cell operating conditions [3, 4]. Moreover, the prolonged SEI growth reduces the accessible active surface area of the negative electrode. That has been measured by impedance rise of the electrodes which is directly linked to the power fade of the cell [5] and the capacity fade of high energy batteries [6].

Contact loss of the active material within the electrodes causes the capacity fade of the cell. It occurs between the graphite particles, between the copper foil current collector and graphite, and between binder and graphite. First of all, the volume of the graphite is expanded about 8% during lithium ion insertion which is a discharge of the cell [7]. The intercalated or deintercalated lithium ions change the molecular structure of the graphite electrode. This compositional inhomogeneity during the solid state diffusion in the active material causes diffusion induced stress (DIS). The mechanical stress might result in cracking or related structural damage that causes contact loss. Secondly, the graphite exfoliation and cracking caused by solvent co-intercalation, electrolyte reduction inside graphite will certainly lead to a rapid degradation of the electrode. Lastly, reactions between the copper foil and electrolyte lead to corrosion of the current contact at low state of charge (SOC) conditions. The corrosion cause electronic and mechanical contact loss between the current collector and the active material. Moreover, the poor electronic conductivity of the corrosion products lead to overpotentials and inhomogeneous potential and current distributions [8].

1.1.3. Cathode Active Material

Lithium cobalt oxide ($LiCoO_2$) is the first commercialized cathode active material. The high energy density, long life time, and low self-discharge of the cell make it attractive cathode material. There are several mechanisms for the positive electrode to cause capacity fading and limited life-time of LIBs.

The structural change during lithium ions insertion or extraction causes DIS in the positive active material, similar to the negative active material. Although there is about 1% of the volume change in the $LiCoO_2$ during the cell operation [9], the repeated DIS causes fatigue failure of the positive active material. Moreover, distortion of the crystal lattice, which enhances the mechanical stress, is caused by phase transition in the positive material. The loss of structural integrity may reduce electric conductance, causing the capacity of the cell to fade [10].

There are also other factors that cause contact loss in the positive electrode such as binder decomposition, oxidation of the conductive material, and corrosion of the current collector. Moreover, the chemical dissolution of the positive electrode material leads to a loss of active material, which is electrically isolated to cause capacity fading. It is considered as a minor factor for the $LiCoO_2$ because a small amount of cobalt is dissolved in the electrolyte [11]. However, the metal dissolution has been reported as a crucial problem for lithium manganese oxide ($LiMn_2O_4$) that leads to capacity loss of the cell [12].

1.1.4. Capacity Loss and Cell Failure

The capacity of commercial LIBs usually decreases after a number of charging and discharging cycles. The capacity fade and lifetime limitation of the LIBs are caused by various mechanisms, such as overcharging, overdischarging, decomposition of the electrolyte, structural instability, etc [1]. For instance, electrolyte decomposition on solid electrolyte interface causes capacity and power fade during first few cycles. And the repeated volume change of the active materials leads to loss of active materials by lithium ion intercalation or deintercalation. However, the degradation mechanism of the LIBs could not be explained with a single reason because it is combined and interacted processes.

The complex mathematical analysis of the LIBs has been studied with many different approaches. For example, Zhang et al applied a multi-scale analysis method for a lithium ion cell [13]. They connected the lithium ion transport in a macro-scale cell and in a micro-scale. This surrogate model suggested a method that simulates a three dimensional (3D) lithium ion transport in a LIB. The model improved the pseudo 2D model [14] by using 3D microscopic particle clusters. However, previous studies assumed the active materials as homogenized material, and spherical particles did not include geometric effects such as porosity and tortuosity of the electrode materials.

Mathematical studies of cell performance, degradation, and failure might be enhanced with realistic microstructure of the electrode materials. Cell failure and capacity loss are highly depend on the local geometry of the materials.

1.2. Literature Review

1.2.1. Diffusion Induced Stress

Diffusion induced stress (DIS) occurs when lithium is intercalated into (or deintercalated from) the electrode particles and it is one of the main reasons of fracture and fatigue failures in the electrode. Fractures in LIB electrodes have been observed on various active materials such as graphite [15, 16], $LiCoO_2$ [17, 18], $LiMn_2O_4$ [19, 20], $LiFePO_4$ [21, 22]. In order to develop strategies to minimize stress-induced battery failure and achieve the lifetime expectation of LIBs, the structural failure mechanisms should be understood theoretically.

Several research groups have studied the DISes in LIB electrodes. For instance, a mathematical model that calculates the stress generated in spherical particles due to lithium intercalation has been developed by Christensen and Newman [7, 23, 24]. They demonstrated the stress generation including a pressure-diffusion term that was accounted

a significant factor for the cycle life of the cells. They formulated a dimensionless current which includes the particle size, charge/discharge rate, and solid state diffusion coefficient of a negative electrode. The maximum DIS in the negative particle has been determined as a function of dimensionless current. They also build up a numerical model for a positive electrode material $LiMn_2O_4$. They compared the simulation results of a two phase material with a one phase material to study the phase change effects during lithium insertion or extraction. They pointed out that the ratio of the two phases is a crucial factor for the DIS besides the particle size and rates. Those models are used to predict fracture in the active electrode material of lithium-ion cells.

Cheng and Verbrugge developed analytic expressions of the DIS and strain energy for a spherical electrode particle [25]. They performed the calculation under galvanostatic and potentiostatic conditions. In a constant current condition, the radial and tangential stresses increased until they reached steady-state values. On the other hand, the stresses were increased initially and then decreased with time in a constant potential condition. Moreover, the strain energy of both simulations showed similar pattern with the stresses. The reason of the different stress evolution was that the stresses were defended on the concentration gradient in the particle. The lithium ion concentration gradient was reached a state-stead value with the constant lithium ion flux on the surface, but the gradient was changed during the lithium insertion process. Based on their results, they suggested a new LIB charging strategy to reduce the stresses.

Zhao et al. introduced a prediction method for the fracture of an electrode material [26]. They combined diffusion kinetics of a LIB and fracture mechanics to quantify the fracture conditions. In their criteria, particle size and material properties were employed to find the effects on the fracture as well as current rates. They estimated the stress and concentration distributions at various discharge rates. Furthermore, they calculated the energy release rates on the pre-existing cracks to compare with the fracture energy. They suggested that the critical particle size and current rate which enable to avoid the mechanical failure of LIB electrodes can be obtained by their criteria.

Zhang et al. have developed a three dimensional finite element model of spherical and ellipsoidal shape particles to simulate DIS [27-29]. They applied Yang's relationship between hydrostatic stress and concentration of solute atoms [30]. They successfully coupled a diffusion equation and stress-strain relationship. In the studies, the 1D coupled equations model estimated the concentration profile with the stress effect and the DIS profile by the concentration gradient. The internal stress gradients accelerate the diffusion. Moreover, they calculated the lithium ion concentration and DIS for 3D spherical particles and 3D ellipsoid particles with different aspect ratio. In their results, increasing particle size and discharge current density enhanced the DISes for the spherical particles. Furthermore, the simulation results of 3D ellipsoidal particles reported that the maximum DIS of the particles is enhanced with increasing the aspect ratios, but it reduced after a certain aspect ratio. The DIS is generated by the concentration gradient in the particle. Thus, the morphology of the particle affected on the concentration and DISes.

1.2.2. Lithium Ion Transport

Mathematical modeling and numerical simulation have been proved to be an effective way to reveal both global and local phenomena that occur on the microstructures of LIBs. Combining with experimental validations, they can give valuable insights into the principles of LIB performances. To this end, comprehensive mathematical models have been developed to simulate the behavior of batteries and reveal the effect of microstructure on the performance of LIBs. At the same time, variant numerical methods are also utilized to analyze correlations between the microstructure and the spatial and time-dependent behavior of LIBs such as galvanostatic charge or discharge, life cycle, thermal effect, and crack distribution.

For instance, Doyle et al. introduced a mean field method which incorporates microstructure into pseudo 2 dimensional model (P2D) [31-33]. P2D treats components of LIB as homogenized material and assumes microstructure of active material as spherical particles. They developed an electrolyte phase transport equation that based on

concentrated solution theory and a material balance equation. They modified the equation for the electrolyte phase in porous electrode by applying the porous electrode theory. Because of its simplicity and concerning microstructure, it has been used widely to simulate discharge or charge processes of LIBs [34-38] including thermal behavior [39-42] and stress analysis [43, 44]. P2D has also been evolved in a capacity fade model of LIB when the solvent reduction reaction and the anode film resistance are incorporated into P2D [45, 46]. Xiao et al. extended P2D to conduct a multi-scale approach for the stress analysis of polymeric separators in a LIB [47].

Renganathan et al. applied a pseudo-2D approach to simulate DIS of porous electrodes. Their model attributed stress buildup within intercalation electrodes to changes in the lattice volume, due to intercalation and phase transformation during the charge/discharge process. [37].

Garcia et al. studied the spatial variations of the electrochemical fields for porous electrode microstructures under galvanostatic control, including DIS [48]. They developed a program to resolve the local particle–particle electrochemical interactions and the performance of LIB with electrode microstructures based on random distributed simple particles [22] and SEM images of LIB electrodes [23].

1.3. Objective of Current Research

Extensive studies have been carried out to model and simulate the DISes of the active electrode particles and the electrochemical phenomenon in LIBs. Most of them are based on the porous electrode theory or simple particle shapes. However, the degradation and failure of the active materials were not sufficiently solved by the numerical simulations that have not detailed geometry information. Moreover, many microscopic studies showed irregular particle shapes, complex microstructures, and mechanical failures [15-22]. Thus, the computational studies are required to consider realistic geometry information which is non-homogeneous and irregular electrode structures.

This study aims to investigate the geometric effects on the electrochemical phenomenon for LIBes. To achieve our goal, we will perform following four objectives in this study.

First of all, the electrode structures of a LIB which has graphite as the anode material and lithium cobalt oxide ($LiCoO_2$) as the cathode material will be reconstructed using x-ray computed tomography technique.

Second, geometrical characteristic of the lithium ion diffusion in electrolyte will be simulated using the reconstructed structures. In terms of tortuosity, the lithium ion transport of electrolyte in cathode and anode site can enhance the understanding of the ion transport phenomena.

Third, DISes will be calculated under galvanostatic conditions using realistic morphologies of electrode particles. By using this approach, more accurate stress development in the LIB electrode particles can be simulated and the simulation results will be very useful to study the capacity loss of LIBs.

Lastly, a finite volume method will be employed to resolve the 3D coupled discharge formulations of an electrolyte-cathode semi-cell using the realistic positive electrode structure. The numerical approach will shows detailed electrochemical phenomenon of LIBs.

2. RECONSTRUCTION OF 3D ELECTRODE STRUCTURES

Many mathematical approaches of lithium ion batteries (LIBs) are based on 1D homogeneous porous electrode models [14, 37, 49] and simple spherical 3D models [7, 24, 27, 28]. Those models have been shown reasonable results with measured material properties and well assumed geometrical characteristic. However, the models encountered to analyze degradation mechanism for LIBs without structural change of the electrodes. Because the 3D morphology of the electrodes affects the lithium ion transport in the LIBs and also the diffusion induced stress in electrode materials. The realistic 3D geometry of the electrode materials is an important factor to enhance the transport simulations and degradation predictions.

Recently, tomographic techniques have been applied to generate 3D structures of porous materials. One of the technique is Focused ion beam-scanning electron microscopy (FIB-SEM) that has been used to generate 3D microstructure for solid oxide fuel cell (SOFC) [50, 51] and a positive electrode of a LIB [52]. Another method is high resolution x-ray computed tomography (CT) that has been applied to obtain 3D morphology of SOFC materials [53] and a negative electrode of a LIB [54].

In this chapter, the method of 3D geometry reconstruction for electrode materials of a LIB will be described using the x-ray CT technique. This non-invasive method can measure the inside structure of the electrodes without any physical interruption which is required to apply FIB-SEM method. Lastly, the geometrical properties will be calculated using the reconstructed 3D microstructures.

2.1. X-ray Projected Image Processing

2.1.1. Principle of Micro/Nano-CT

X-ray computed tomography (CT) is a technology to generate a three dimensional (3D) image of inside of an object from a large series of 2D x-ray images. The x-ray CT technology can be applied various areas where need to generate the inside structure without any physical interfering such as medical imaging for screening disease or preventive medicine. Furthermore, the non-destructive advantage of the x-ray CT system enables a functional material to be reconstructed its internal structure. However, conventional x-ray point projection can generate around 0.25 μm spot size because of the limitation of a transmission x-ray laboratory source [55]. Fortunately, the novel lens based nano-CT provides far superior spatial resolution which is around 50 nm. The schematic of the Nano-CT configuration is depicted in Figure 2.1.

This configuration is similar to the high resolution x-ray microscopes at synchrotron light sources which utilizes Fresnel zone plates as objective lenses. A nanoscale 2D image is generated through following steps. Firstly, filtered laboratory x-ray sources will be compensated for the lack of flux through a high efficiency reflective capillary condenser lens. The x-rays penetrate an object through as much as 100 μm that the sample thickness limitation is depended on the material. Second, Fresnel zone plates focus x-rays by means of diffraction to make high a resolution image. The resolution of the zone plate based x-ray microscope is independent of x-ray source spot size and is ultimately limited by the outermost zone width of the zone plate which means that finer zones give higher resolution. Third, the phase ring increases the contrast in transmission x-ray imaging for low Z materials. After that, the x-rays arrive on the scintillator detector and are projected on the CCD. Lastly, the sample object is rotated at 0.5° rotation increment over 180° to capture a 2D nanoscale image. Those steps are repeated at different heights until to measure the whole sample. Micro-CT is a solution for a large

sample. It can generate the inside structure of the sample (up to several millimeters) with a high resolution.

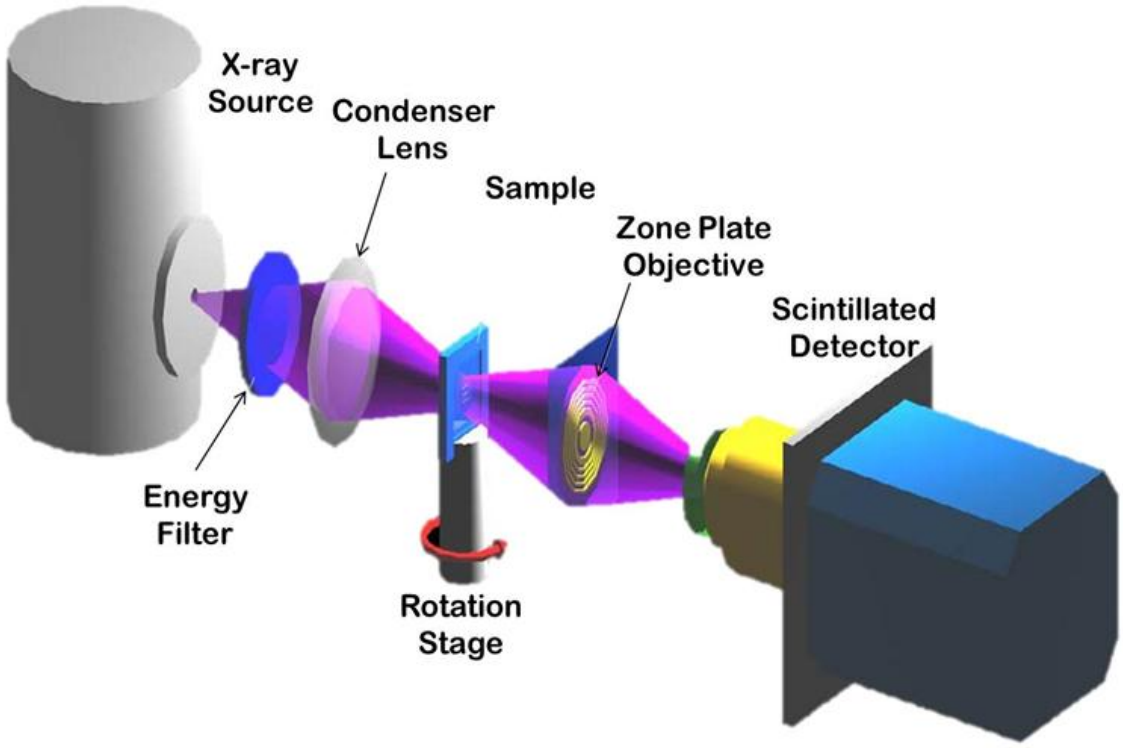

Figure 2.1 Schematic of nanoXCT 3D X-ray microscope with specialized highly efficient reflective condenser, Fresnel Zone plate optics and high resolution imaging detector

2.1.2. Sample Preparation

To obtain sample anode and cathode electrodes, a commercial lithium ion battery (SP035518AB, Tianjin Lishen Battery Co., Tianjin, China) was disassembled in an argon filled glove-box. The lithium ion battery is showed in Figure 2.2 (a). Figure 2.2 (b) showed the positive electrode material which is attached on an aluminum foil. A piece of positive electrode ($LiCoO_2$) and a piece of negative electrode (graphite) were collected to separate from their current collectors. Because the aluminum and copper current collectors on the electrodes can affect the CT scans, they need to be removed from the sample electrodes. The aluminum current collector and the attached $LiCoO_2$ electrode

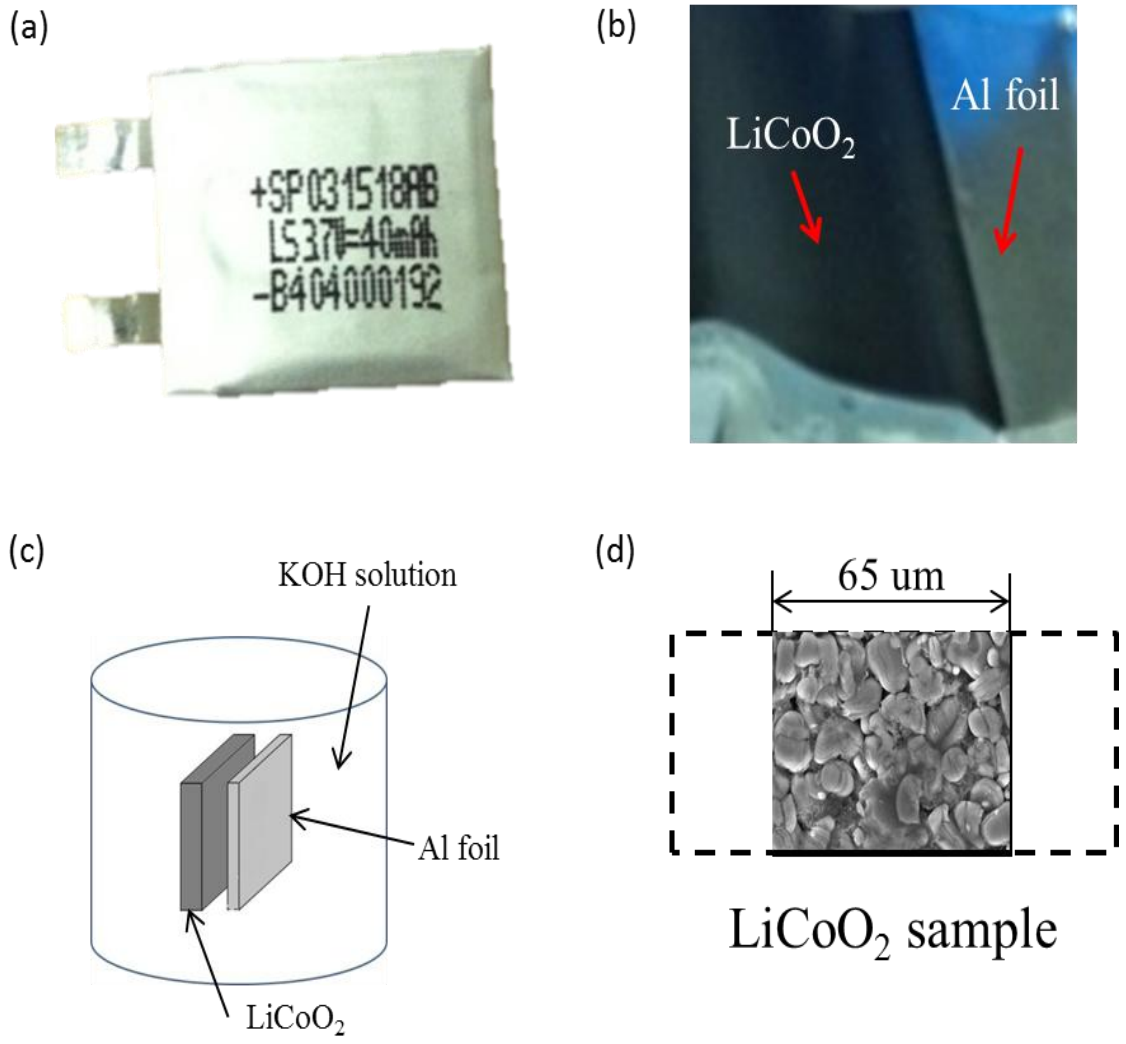

Figure 2.2 Sample preparation process for the positive electrode (a) a commercial lithium ion battery (SP035518AB, Tianjin Lishen Battery Co., Tianjin, China), (b) disassembled positive electrode in the glove-box, (c) delaminating the current collector, and (d) a 65 μm slice of the positive active material

were delaminated by soaking in a 30% KOH solution for 3 min. The copper current collector was etched by nitric acid to obtain the negative active materials in Figure 2.2 (c). The positive electrode was cut in a 65 μm slice as a sample for the nano-CT scan in Figure 2.2 (d). In negative electrode case, the sample was prepared in a 1 mm slice for the micro-CT scan.

2.1.3. Projected Images

An Xradia nanoXCT-100 system (Xradia, Pleasanton, CA) was employed for high resolution computerized tomography of the positive active materials. Because the x-ray absorption rate of carbon is much lower than that of $LiCoO_2$, an Xradia microXCT-200 system was employed for the negative active material. Projected X-ray images were acquired at 0.5 °rotation increments over 180 °.

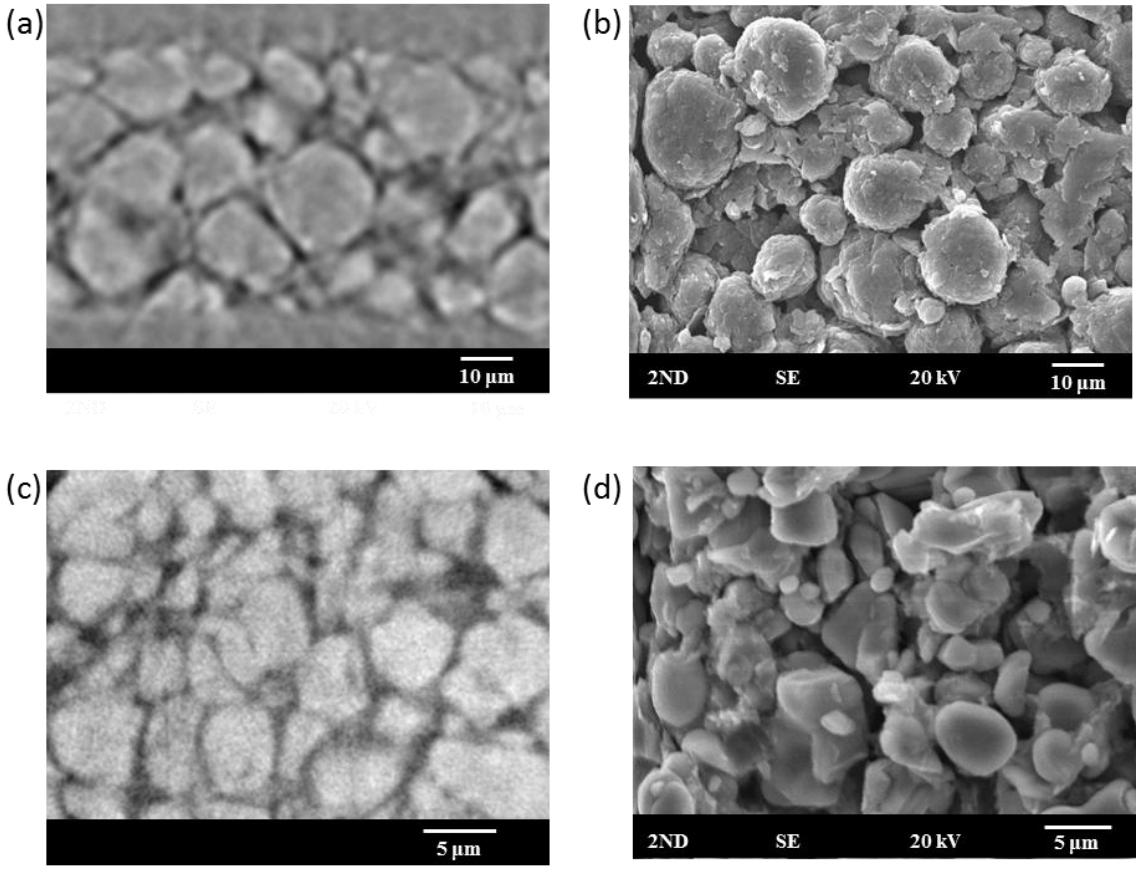

Figure 2.3 Different morphology images of active materials from a commercial lithium ion battery, (a) nano-CT image and (b) SEM image of $LiCoO_2$, (c) micro-CT image and (d) SEM image of LiC_6

Data collection is fully automated with 2 min/projection exposure time in order to obtain data with a good signal to noise ratio. A raw projection data of the positive active material from nano-CT corresponding to 64 nm pixel dimension is shown in Figure 2.3 (a). The light colored phase is regarded as the positive active material, while the rest of the image is regarded as empty volume for electrolyte. As seen from Figure 2.3 (b), the

2D geometry of the $LiCoO_2$ electrode shows similar patterns with its SEM image which was measured by a scanning microscope (JSM-5310LV, JEOL Ltd). $LiCoO_2$ particles have irregular shapes with particle size range from 3 to 5 μm. A raw projection data from micro-CT corresponding to 560 nm pixel dimension in Figure 2.3 (c) and a SEM image of the negative material are shown in Figure 2.3 (d). Both images show the similar negative particle size range from 5 to 20 μm.

2.1.4. 3D Morphology Reconstruction

Scanned images of active materials were imported to the commercial software MIMICS (Materialise HQ, Leuven, Belgium) in Figure 2.4 (a). For the positive electrode, 500 of raw x-ray projected images which have a 56 nm pixel resolution were employed to reconstruct the 3D morphology of the electrode with a 56 nm distance between the each image. Figure 2.4 (b) shows processed 3D image of the positive electrode in MIMICS. The gray colored raw data were modified in black and white images which enable to divide off the electrode material of the images. Figure 2.4 (b) shows processed 3D image of the positive electrode in MIMICS.

A part of the area where represents the positive electrode was selected to generate the 3D structure to reduce the computational time. Figure 2.4 (c) shows the reconstructed positive electrode structure that has a through plane thickness of 19.584 μm, a width 20.032 μm, and a height 20.032 μm. The volume of the reconstructed positive electrode structure is a 6,384.62 μm^3. In negative electrode case, 300 generated raw images by micro-CT were imported with a 0.64 μm distance in MIMICS. The reconstructed 3D morphology of the negative electrode is shown in Figure 2.4 (d). That has a through plane thickness 40.32 μm and a 39.76 × 39.76 μm^2 cross section. It has a 42,366.55 μm^3 negative electrode volume.

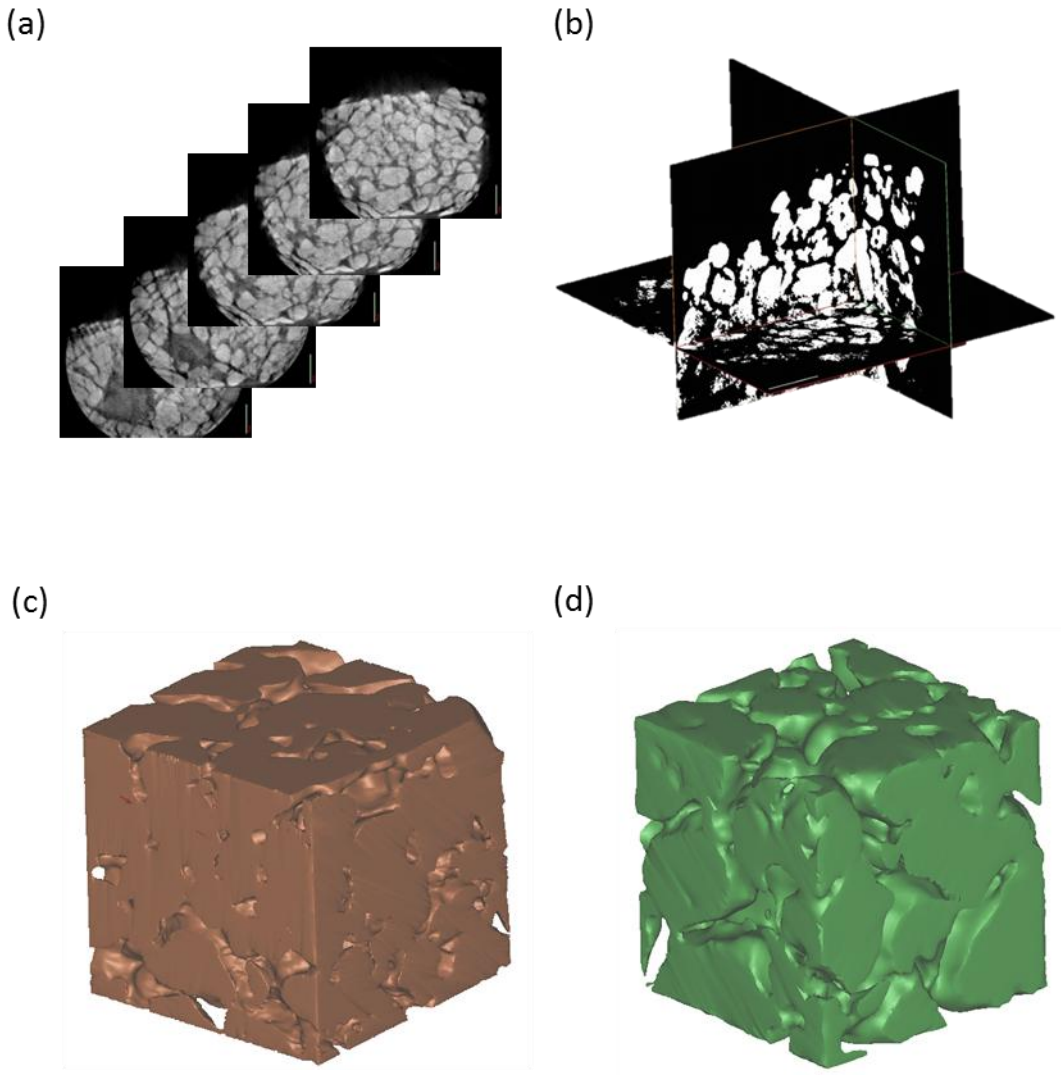

Figure 2.4 Three dimensional reconstructed electrodes (a) imported raw projected positive images in MIMICS, (b) modification of the raw data, (c) the 3D structure of $LiCoO_2$, and (d) the 3D structure of graphite

The reconstructed microscale structures include electric conductive and binder materials as well as active electrode materials. However, x-ray projected images had not enough information to extract only the active material which has an 85~90% weight ratio. We assumed that the 3D morphology of the positive electrode as a $LiCoO_2$ and the 3D geometry of negative electrode as a graphite.

2.2. Geometrical Characteristic of Reconstructed Structure

Until now, computational studies about LIBes have been achieved remarkable improvements. Many studies were adopted the porous electrode theory [49] which incorporates microstructure into a pseudo 2 dimensional model. The porous electrode theory describes the porous electrode by its specific interfacial area and volume fractions of each phase instead of the pore geometry. As shown in Figure 2.4 (c) and (d), the reconstructed electrode geometries are highly complicate structures in microscale. Thus, the study of the reconstructed microstructure facilitates a realistic analysis of the LIBes. In this section, geometric characteristic will be clarified for the reconstructed microstructures.

2.2.1. Local Porosity and Tortuosity

Porosity is a volume fraction of the void volume over the total volume. The void space of porous electrodes is filled with liquid electrolyte in LIBes. The porosity of electrodes is considered a crucial parameter that determines capacity and power density of the LIBes. Usually, a LIB has a high capacity density with a low porosity which means more active material in the cell. However, high porosity leads a high power density because fast lithium ion transport is possible in the spacious electrolyte.

Tortuosity is a geometric parameter of curve being tortuous [56]. It is considered as a limitation to mass transport in porous materials. Bruggeman relationship often used to quantize the tortuosity of a porous medium. The relationship is given by

$$\tau = \varepsilon^{1-\alpha} \tag{2.1}$$

where α is the Bruggeman coefficient.

There are various approaches to estimate tortuosity [57-60]. For example, Hutzenlaub et al. evaluated the tortuosity using an electrical resistivity model for a reconstructed electrode geometry [61]. Their suggested tortuosity was described as a linear function of porosity with a formation factor that estimated based on the empirical

effective electric conductivity of the porous electrode. Kehrwald et al. have developed a numerical method to obtain the tortuosity including a 3D morphology of a porous structure [62]. In this research, Kehrwal's model is adopted for our reconstructed positive and negative active material structures. Thorat et al. measured effective electrolyte transport in porous LiFePO4 electrode using polarization-interrupt experiment. They pointed out that the tortuosity difference between their empirical result and Bruggenman relationship [63].

2.2.2. 3D Electrolyte Phase Morphology

To calculate the tortuosity of the 3D reconstructed electrode structures, lithium ion path ways in the LIB is generated by selecting non-active material area in MIMICS. Figure 2.5 (a) shows a microstructure of positive electrolyte phase that has a dimension 19.584 μm × 20.032 μm × 20.032 μm. A reconstructed negative electrolyte phase is shown Figure 2.5 (b). The structural dimension is a 40.32 μm × 39.76 μm × 39.76 μm.

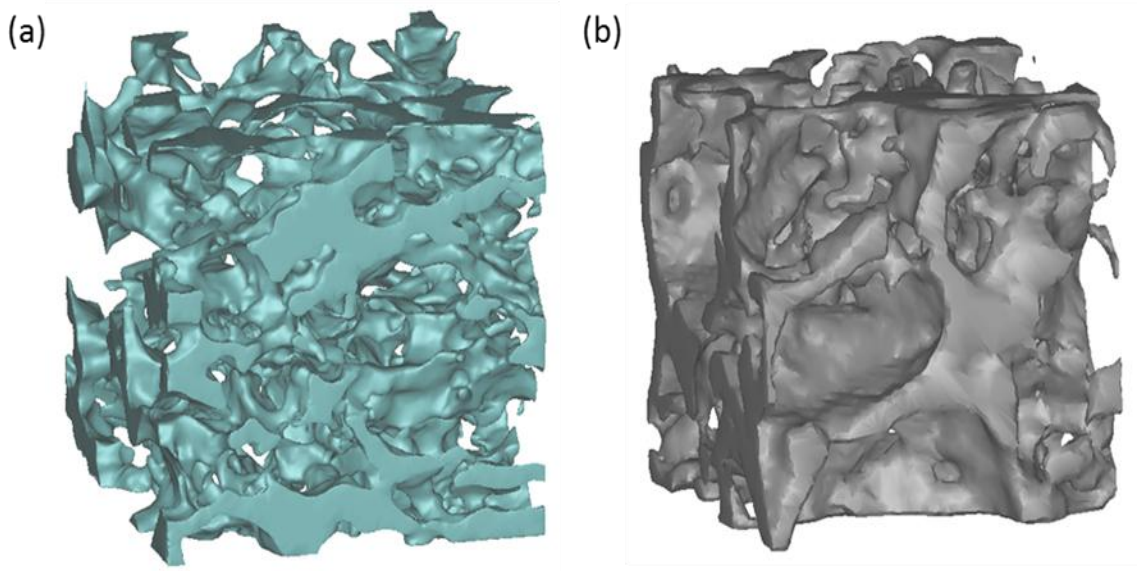

Figure 2.5 Reconstructed electrolyte phase microstructures (a) a positive site and (b) a negative site in MIMICS

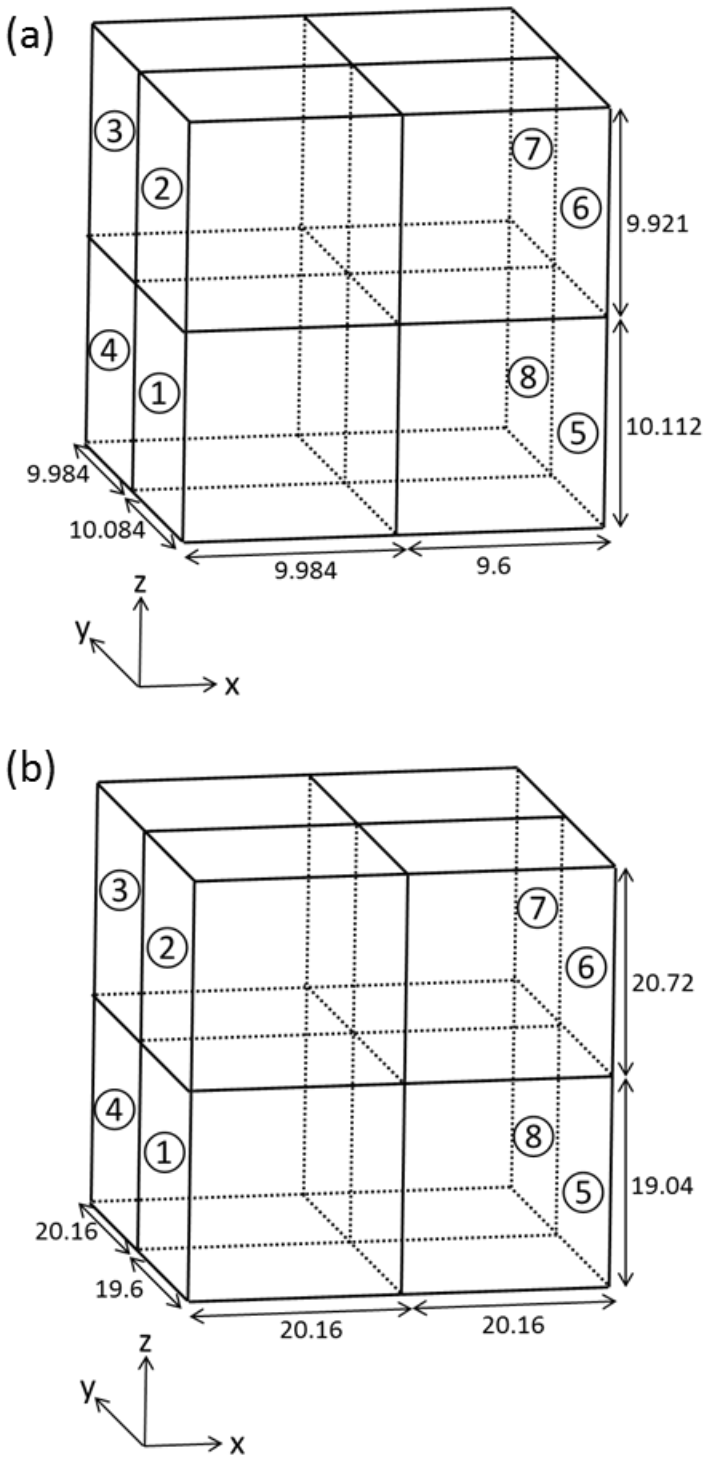

Figure 2.6 Sub-division of the microstructures (a) the positive and (b) the negative electrolyte site

The both microstructures are divided in 8 sub-divisions to analyze the local geometrical effects on diffusion. Figure 2.6 describes the sub-divisons of the positive and negative microstructures.

2.2.3. Mathematical Model

Tortuosity is a geometric characteristic of a 3D structure. A linear diffusion equation was applied to describe the transport in a complicated porous structure [62]. The equation is given by

$$D\Delta c = 0 \tag{2.2}$$

where D is the diffusion coefficient and c is the concentration of a given species. We assume the diffusion coefficient as a $1m^2/s$ in this model. Tortuosity is independent on the species which is diffused in the structure.

Boundary conditions of the tortuosity model are described in Figure 2.7. There are two constant concentration conditions at X_1 and X_2 boundaries. The other four boundary planes are applied an open boundary condition.

From the diffusion model, the mass flow late was obtained in x direction. The equation is given by

$$\dot{m} = A_{pore}(x)n \cdot D\nabla c \tag{2.3}$$

where $A_{pore}(x)$ denotes the cross section area of the electrolyte phase structure. The mass flow rate is not depend on a position x in steady state diffusion. Thus, the constant mass flow rate through the x direction can be written in the form

$$\dot{m} = \frac{A_{eff} \cdot D_{eff}}{x_2 - x_1} \tag{2.4}$$

where A_{eff} is the effective surface area that has a value of $(y_2\text{-}y_1)\times(z_2\text{-}z_1)$, and D_{eff} is the effective diffusion coefficient. In general, the effective diffusion coefficient is obtained by

$$D_{eff} = \frac{D\varepsilon}{\tau} \tag{2.5}$$

where ε is the porosity and τ is the tortuosity. Tortuosity of the electrolyte phase structure can be obtained from the Equation 2.4 and Equation 2.5. As a consequence the tortuosity is given by a following Equation 2.6.

$$\tau = \frac{A_{eff} D \varepsilon}{\dot{m}(x_2 - x_1)} \tag{2.6}$$

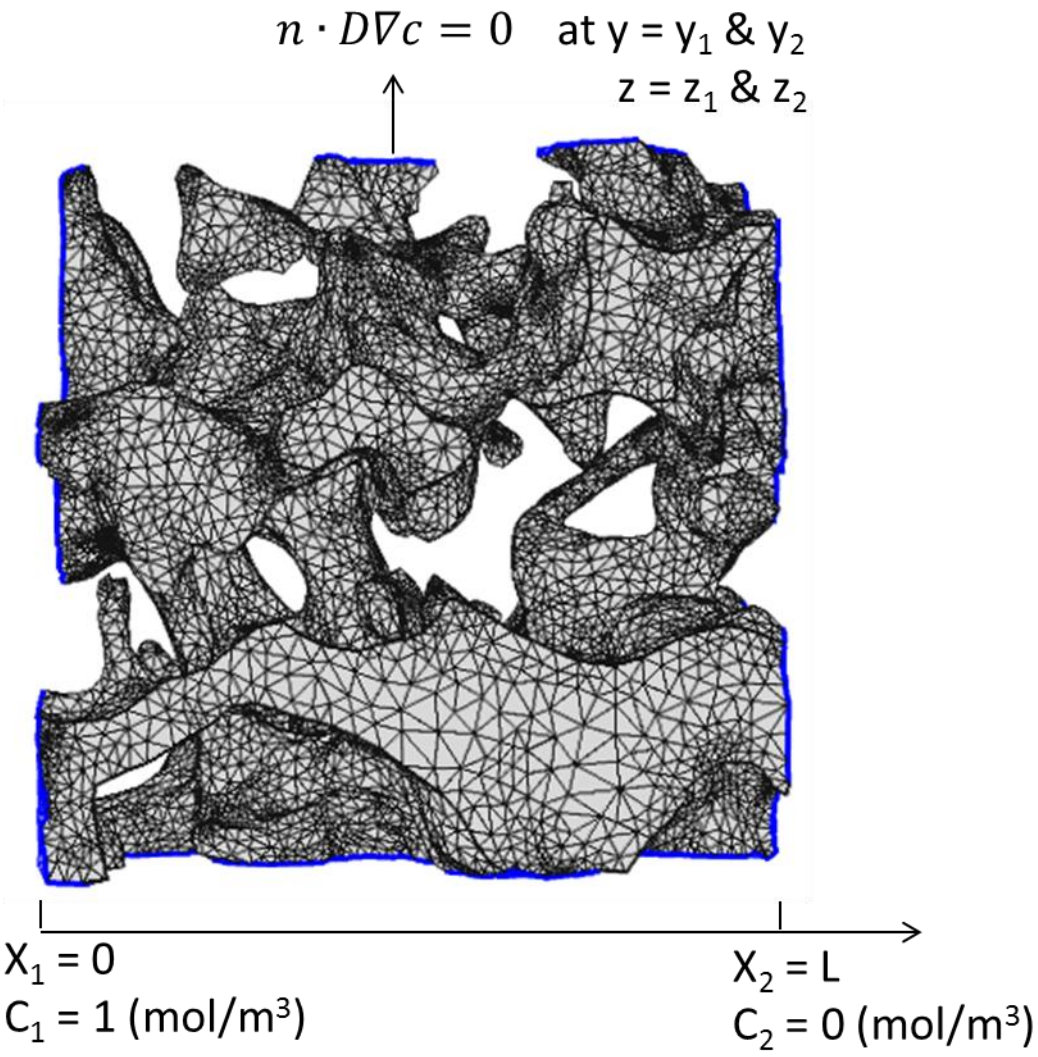

Figure 2.7 Boundary conditions of the tortuosity diffusion model

2.2.4. Results and Discussions

The diffusion simulation was solved for the each sub-division geometry of reconstructed positive and negative electrolyte sites in COMSOL Multiphysics 4.1a. The porosity of the geometry was obtained from the volume of the electrolyte site structure divided by the whole volume that includes the electrode site as well as the electrolyte site. The mass flow rate which was calculated from the sub-division simulation was applied in Equation 2.5 to obtain the tortuosity of the geometry.

As results of the positive electrolyte structure, the porosity of the sub-divided geometries is shown in Figure 2.8 (a). The result shows that the sub-division 2 has the highest porosity 0.258, the sub-division 8 has the lowest porosity 0.128, and the average porosity is a 0.187. Figure 2.8 (b) shows the sub-division tortuosity. The tortuosity of the sub-division 4 has the highest value 9.555 and the tortuosity of the sub-division 5 has the lowest value 2.484. If the local geometric affects are ignored, the tortuosity decreased with increasing porosity by the Bruggeman relationship. However, the simple relationship between porosity and tortuosity does not explain the results of sub-division 4 and 5 without the geometric characteristic of the sub-divisions.

Figure 2.9 shows the (a) porosity and (b) tortuosity results for negative reconstructed sub-divisions. The sub-division 5 has the maximum porosity 0.997 and the sub-division 8 has the minimum porosity 0.281. The average value of the porosity is 0.335. The large particle size of the graphite particle (5~20 μm) causes higher porosity of the negative site. The tortuosity difference between sub-division 3 (2.297) and 4 (2.063) those have similar porosity is not explained without the local morphologies.

In porous electrode theory, the tortuosity of electrodes is estimated by a porosity and Bruggeman coefficient (α). To compare our results with Equation 2.1, we estimate α using the average porosity and tortuosity values. The positive Bruggeman coefficient is α=1.935 and negative Bruggeman coefficient is α = 1.727. Figure 2.10 shows the porosity

and tortuosity correlations in Figure (a) and (b). We also draw the correlation data with α = 1.5 that is often used in LIB simulations.

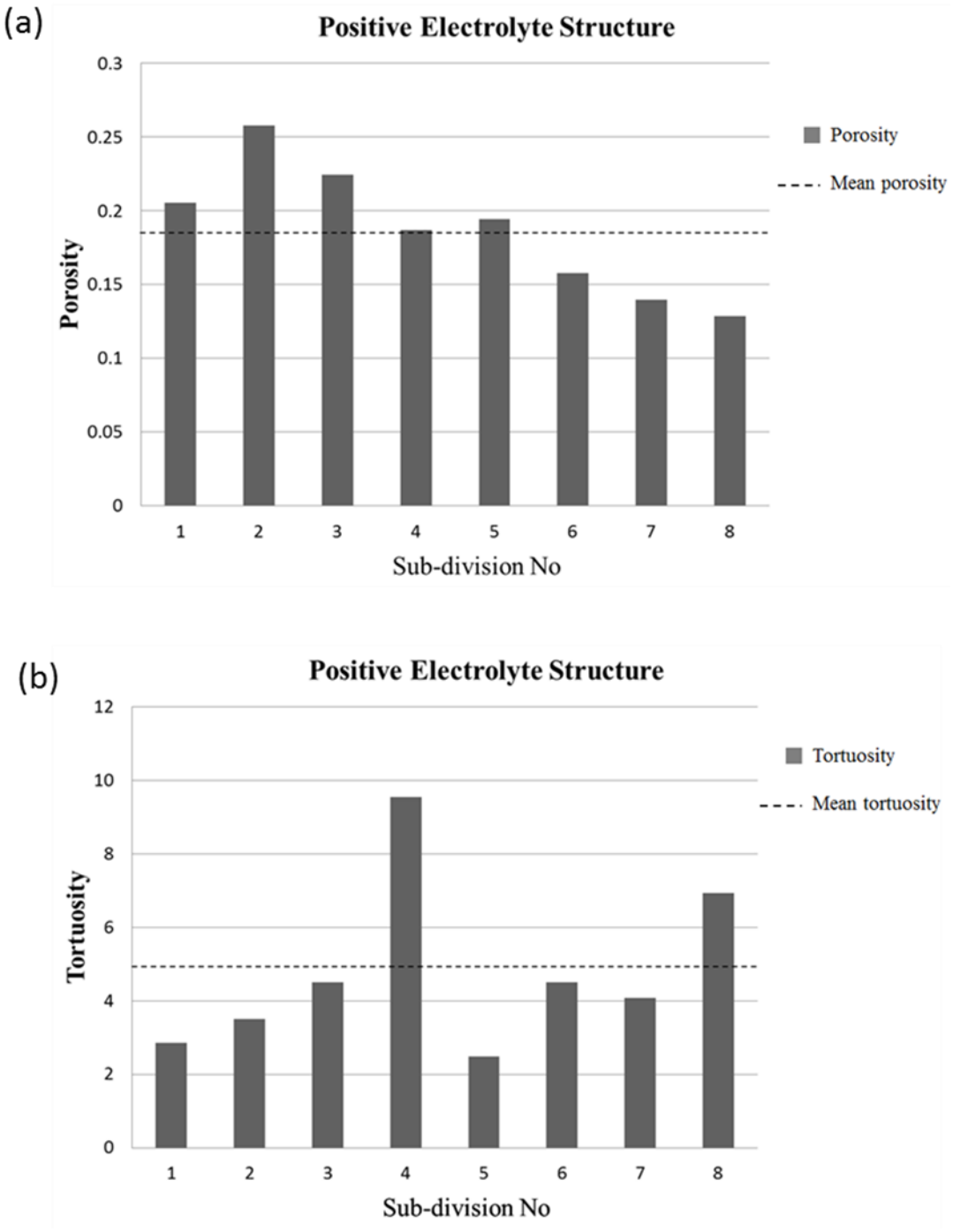

Figure 2.8 Positive reconstructed electrolyte site (a) porosity and (b) Tortuosity

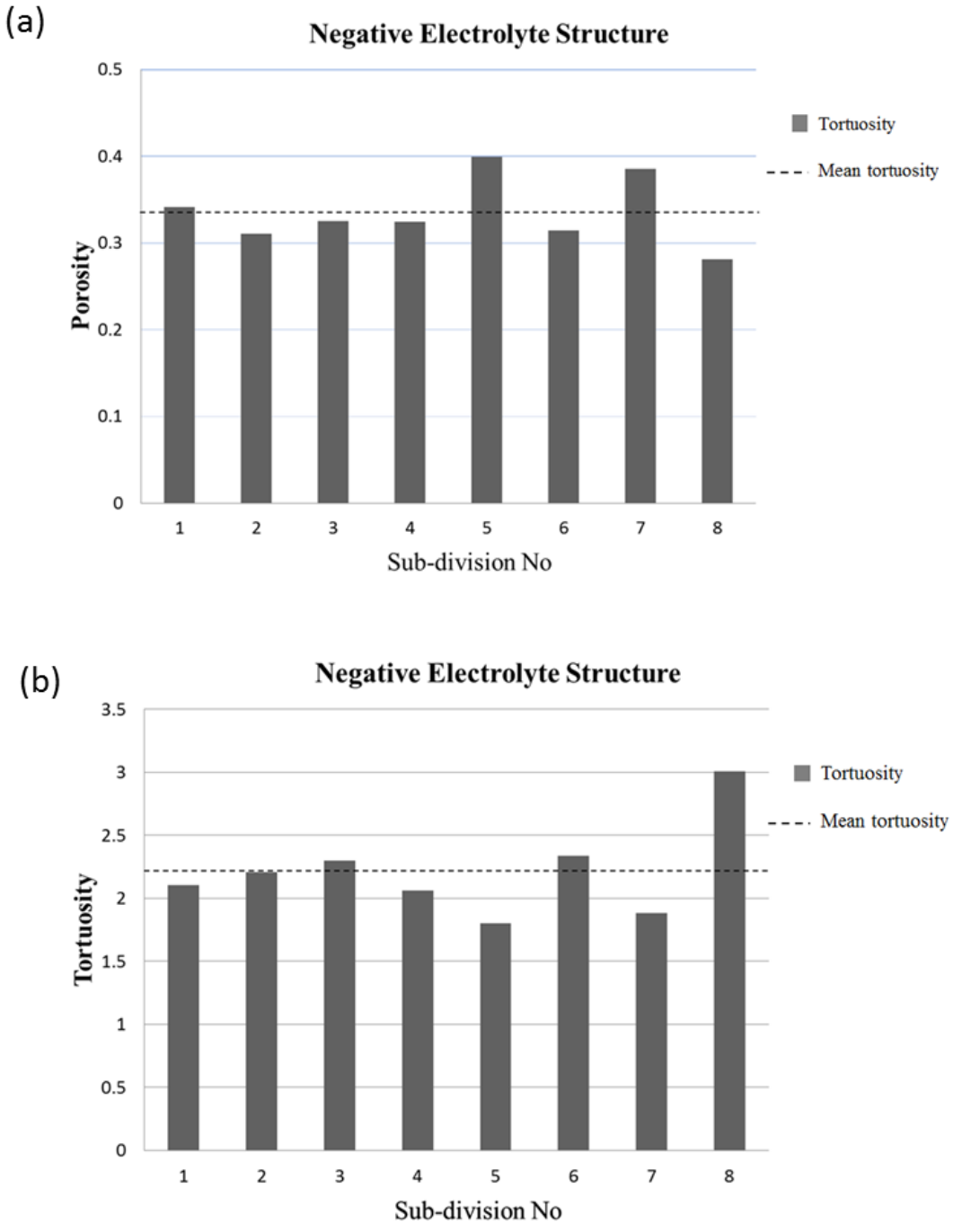

Figure 2.9 Negative reconstructed electrolyte site (a) porosity and (b) Tortuosity

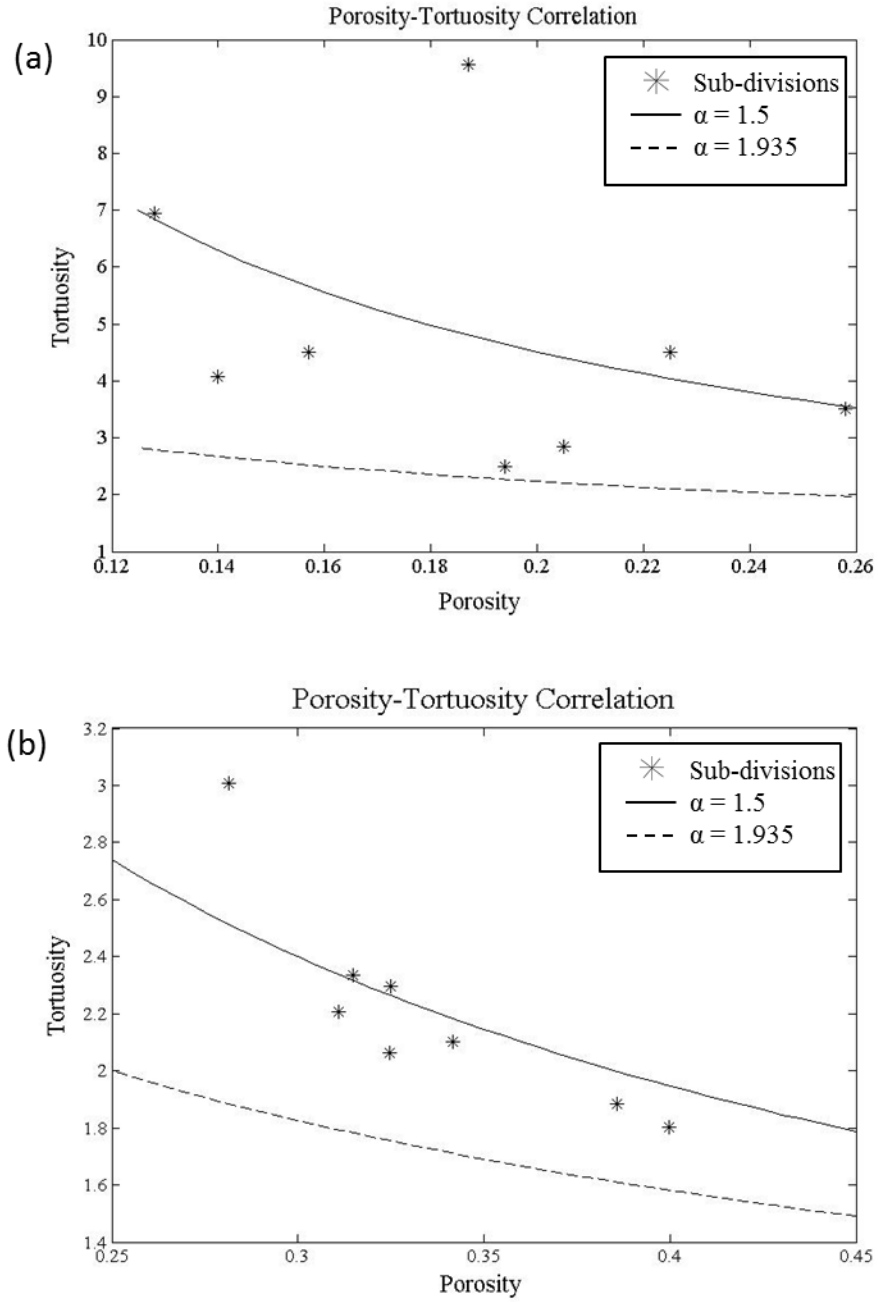

Figure 2.10 Porosity-tortuosity correlations for (a) positive and (b) negative sites

3. DIFFUSION INDUSED STRESS IN ELECTRODE PARATICLES

This study aims to investigate the DISes under galvanostatic conditions using realistic microstructures of electrode particles generated by x-ray micro/nano-CT technology. By using this approach, more accurate stress development in the LIB electrode particles can be simulated and the simulation results will be very useful to study the capacity loss of LIBs. In this work, electrode samples from a commercial lithium ion battery will be scanned using x-ray micro/nano CT. The three dimensional morphology of LIB electrodes will be reconstructed based on a set of two dimensional projected images by the commercial software MIMICS. The DISes in realistic microstructures will be simulated and compared with those in spherical particles.

3.1. Mathematical Model

In this study, the lithium ion transport in both negative and positive electrode particles will be simulated by solving two coupled equations. These equations include a diffusion equation with hydrostatic stress effect and stress-strain relations with a lithium ion concentration term [27].

The stress-strain relationship including lithium ion intercalation effects is obtained by analogy to thermal stress. The temperature change term in the thermal stress-strain equation is replaced by concentration change. The equation is given by

$$\varepsilon_{ij} = \frac{1}{E}\left[(1+\nu)\sigma_{ij} - \nu\sigma_{kk}\delta_{ij}\right] + \frac{\breve{c}\Omega}{3}\delta_{ij} \tag{3.1}$$

where ε_{ij} are strain components, σ_{ij} are stress components, E is Young's modulus, ν is

Poisson's ratio, δ_{ij} is the Kronecker delta, č = c – c_0 is the lithium ion concentration change from the initial value, and Ω is partial molar volume of the active material.

The diffusion process in active materials is described by the following equation

$$\frac{\partial c}{\partial t} = \nabla \cdot D\left(\nabla c - \frac{\Omega c}{RT} \nabla \sigma_h \right) \tag{3.2}$$

where c is the concentration of lithium ion in an active material particle and D is the diffusion coefficient. R is the gas constant, T is absolute temperature, and Ω is the partial molar volume of the active material. σ_h is the hydrostatic stress, which is defined as $\sigma_h = \sigma_{ii}/3$ (where σ_{ii} are the elements in stress tensor).

The boundary condition of the diffusion equation is applied by

$$-\nabla \cdot D\left(\nabla c - \frac{\Omega c}{RT} \nabla \sigma_h \right) = \frac{i_n}{F} \tag{3.3}$$

where i_n is the current density on the particle surface and F is Faraday's constant.

3.2. Diffusion Induced Stress Simulation

A solid mechanics module for the stress-strain relations and a partial differential equation module in COMSOL Multiphysics 4.2 were utilized to simulate the DIS in active material particles. The reconstructed particles were imported as a geometric shape of active materials and meshed to the tetrahedral elements in COMSOL. The current density of each reconstructed particle was obtained from the surface area, the volume of the particles, and the specific density of materials.

A reconstructed graphite particle which has a volume of 4474.4 μm^3 is shown in Figure 3.1 (a). The realistic particle shape shows complex geometry with convex and concave regions. For comparison, a spherical particle with the same volume is simulated in this study, which has a corresponding radius of 10.22 μm. Three other realistic

reconstructed particles (one graphite particle and two $LiCoO_2$ particles) are shown in Figure 3.2 and the corresponding boundary conditions are listed in Table 3.1.

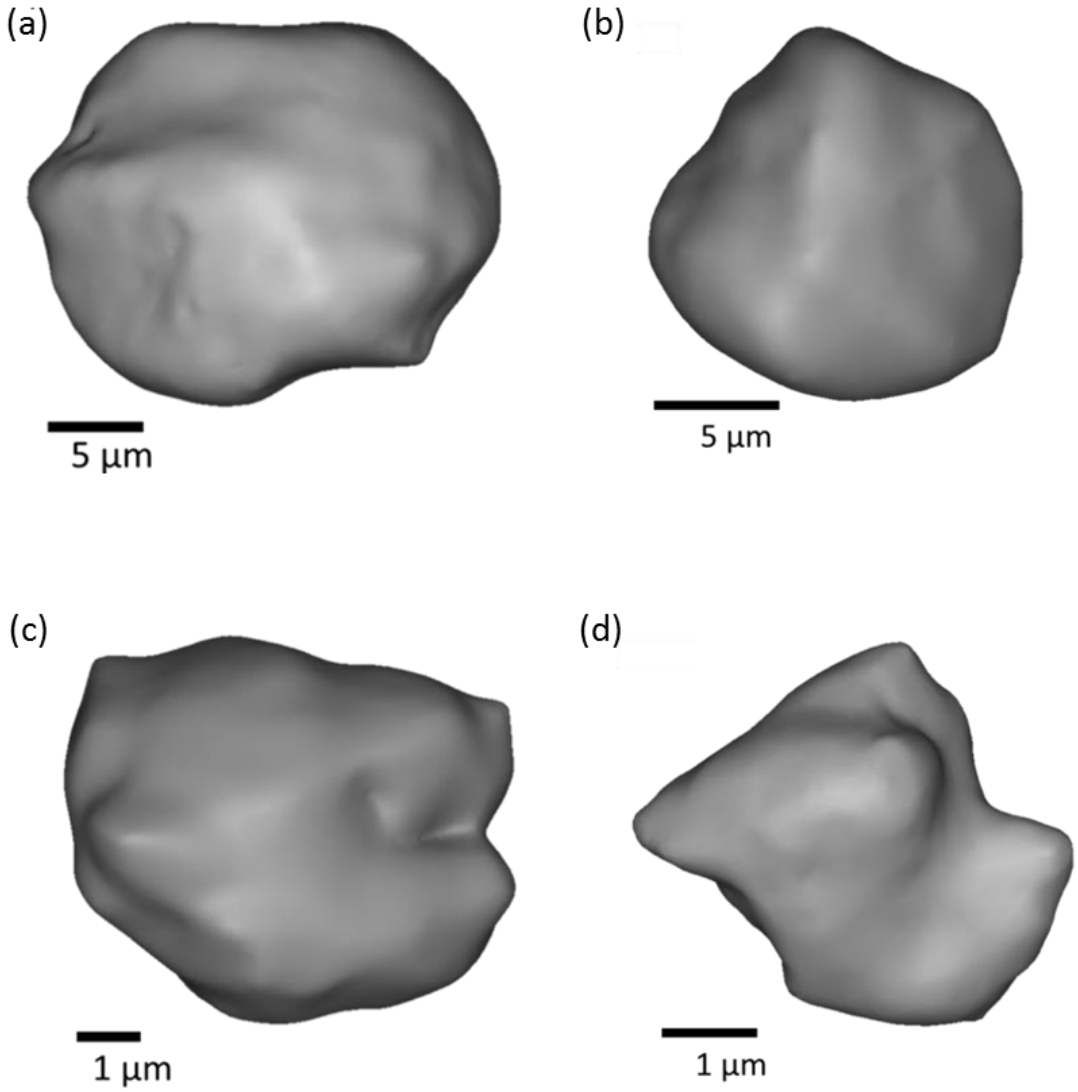

Figure 3.1 Reconstructed three dimensional microstructure of LiC_6 and $LiCoO_2$ particles from micro/nano-CT scans, (a) LiC_6 particle 1, (b) LiC_6 particle 2, (c) $LiCoO_2$ particle 3, and (d) $LiCoO_2$ particle 4

Parameters used in the simulations are listed in Table 3.2. In the present work, the active materials were assumed as isotropic materials, even if they had single crystal structure in molecular level. The volume expansion of the negative active material is 14%

from C_6 to LiC_6 after fully charging [7, 64], and the volume contraction of the positive active material is 1.07% from $Li_{0.4}CoO_2$ to $Li_{0.95}CoO_2$ after discharging [9]. The other assumption is that the volume expansion or contraction of the active materials is considered to change linearly with the lithium ion concentration of the materials.

Table 3.1 Reconstructed particle list

	Surface Area (μm^2)	Volume (μm^3)	Radius (μm)	1C Rate (A/m^2)	Material
Particle 1	1386.2	4474.4	10.22	2.64	LiC_6
Particle 2	641.9	1389.0	6.92	1.77	LiC_6
Particle 3	128.6	120.4	3.06	0.66	$LiCoO_2$
Particle 4	36.6	15.9	1.56	0.31	$LiCoO_2$

Table 3.2 List of material properties

Parameter	Symbol and dimension	LiC_6	$LiCoO_2$	Reference
Young's modulus	E (GPa)	15	70	[37]
Poisson's ratio	N	0.3	0.2	[7, 9]
Partial molar volume	Ω	3.334×10^{-6}	-3.852×10^{-7}	[7, 9]
Maximum concentration	C_{max} (mol/m^3)	31,858	49,943	[41]
Diffusion coefficient	D (m^2/s)	2.62×10^{-14}	1×10^{-13}	[37]
Molecular mass	M (g/mol)	78.64	97.8	[65]
Density	ρ (g/m^3)	2.2×10^6	5.16×10^6	[66]

3.3. Results and Discussions

Under a galvanostatic condition, reconstructed particles are assumed to have uniform current densities on their surfaces and they were simulated to find the DISes. The corresponding spherical particles were also simulated to make the comparison. The graphite particles (Li_xC_6) were charged at different C rates during the average state of charge (SOC) from 0 to 0.9, while Li_yCoO_2 particles were discharged at different C rates during the average SOC from 0.5 to 0.95.

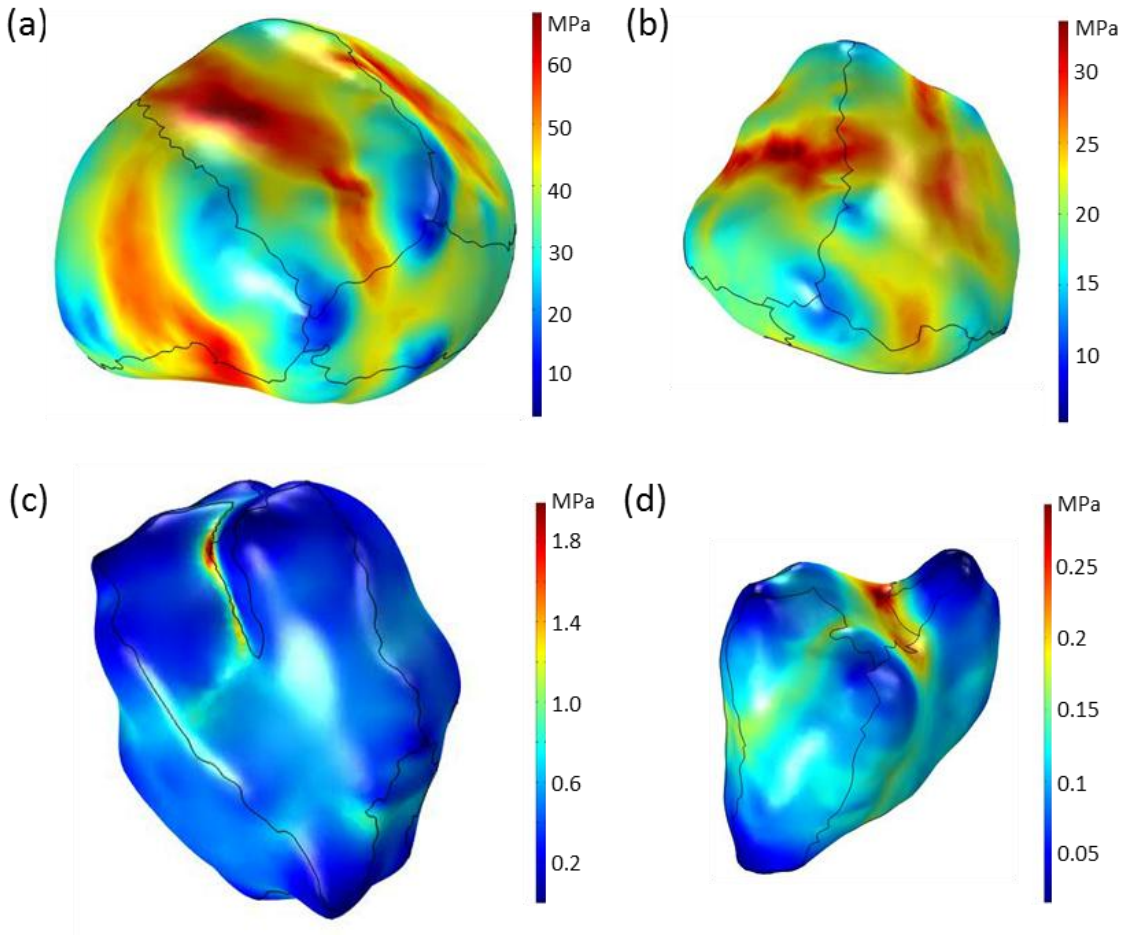

Figure 3.2 Von Mises stress distribution on the surface of active material particles with 1 C intercalation condition, (a) LiC_6 particle 1 at 480 s, (b) LiC_6 particle 2 at 290 s, (c) $LiCoO_2$ particle 3 at 110 s, and (d) $LiCoO_2$ particle 4 120 s

In Figure 3.2, the DISes of negative and positive active materials are displayed in terms of von Mises stress when they reach the highest stresses at certain positions in the particles. Figure 3.2 (a) shows the stress profile of LiC_6 particle 1 with a 1 C intercalation process at 480 s (SOC: 0.133) when the maximum stress is reached. The highest von Mises stress is 68 MPa in the concave area and the convex area has relatively low stresses. In Figure 3.2 (b), particle 2 shows a similar von Mises stress distribution, but the highest stress is 33.4 MPa at 290 s (SOC: 0.081). DIS is usually higher in larger particles because the applied lithium ion intercalation rate on the surface of particles is dependent on their surface to volume ratio. As shown in Table 3.1, at the same C rate, large particles have lower surface to volume ratio and higher intercalation rate, thereby resulting higher DIS. Figure 3.2 (c) and (d) show the von Mises stress results of particle 3 at 110 s (SOC: 0.531) and particle 4 at 120 s(SOC: 0.533). Similarly, the concave areas of the $LiCoO_2$ particles experience higher DIS than the convex areas. However, the stresses in the $LiCoO_2$ particles are much lower than the LiC_6 particles because of diminutive particle size, small partial molar volume of $LiCoO_2$, and high lithium ion diffusion coefficient in $LiCoO_2$ particles [7]. High lithium ion diffusion coefficient can cause rapid lithium ion diffusion in active materials. According to Equation 3.1, the DIS is decreased in a small lithium ion concentration gradient caused by fast diffusion. The results of coupled equations demonstrate that the diffusion-induced stress of active materials is determined by the morphology, size, and material properties of the particles.

In order to demonstrate the geometric shape effects on the lithium ion concentration and the stress, particular points A, B, C, and D are selected on the surface of particle 1. The position and morphology of the selected points are displayed in Figure 3.3 (d). The lithium ion concentration at 480 s (SOC: 0.133) with 1 C intercalation is shown in Figure 3.3 (a). Point A is located on a concave area, and it has 4980 mol/m3 lithium ion concentration. The lithium ion concentrations of the convex area have different values at point B (6000 mol/m3), point C (6120 mol/m3), and point D (6850 mol/m3). The large curvature of the convex area tends to lead to high lithium ion concentration, because the surface to volume ratio is relatively large with the large

curvature. The von Mises stresses and Tresca stresses at four points are shown in Figure 3.3 (b) and (c). The surface of the particle experienced higher overall DIS than its inside during galvanostatic intercalation [27] because of the large lithium ion concentration gradient on the surface. The highest von Mises stress is located at point A (68 MPa), and the lowest stress is located at point D (20 MPa).

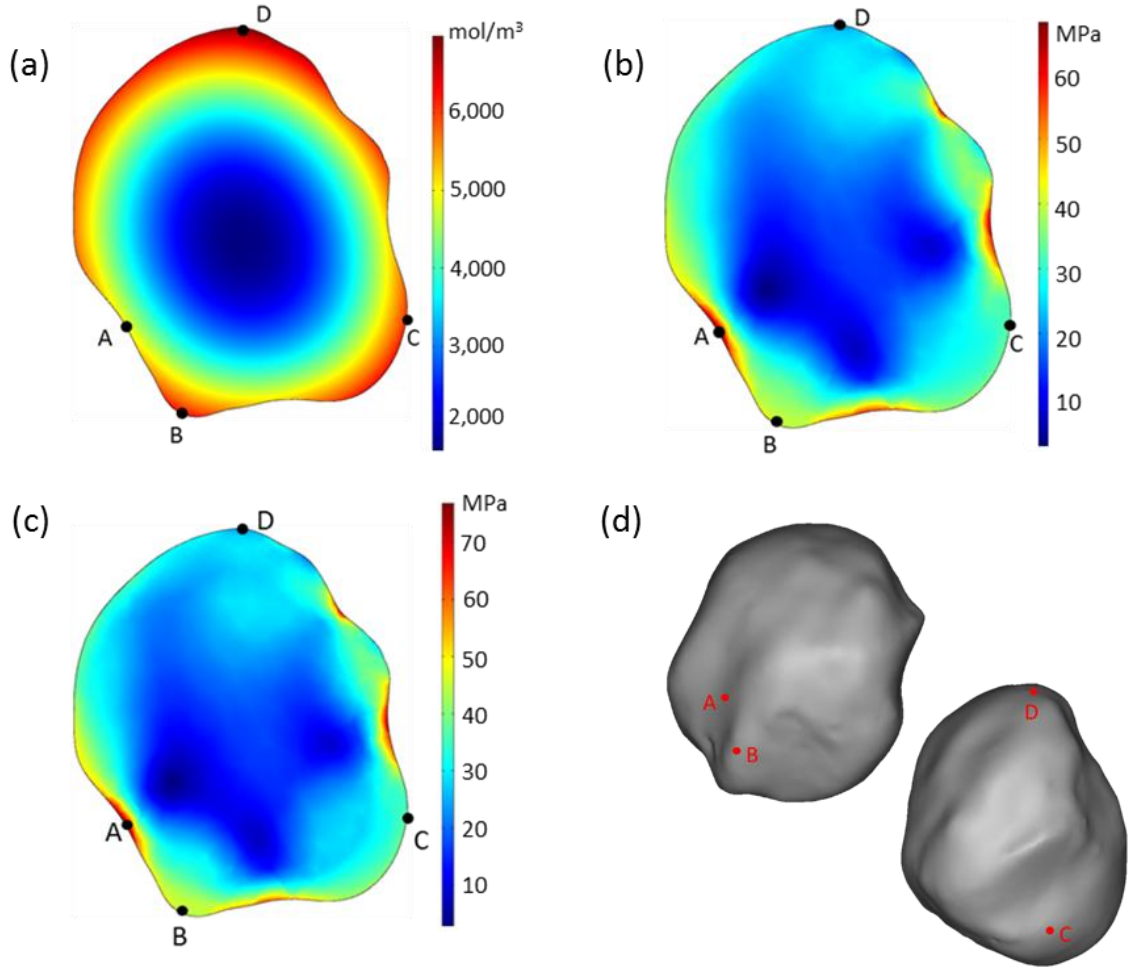

Figure 3.3 Simulation results of LiC_6 particle 1 at 480 s with 1 C intercalation condition, (a) concentration, (b) von Mises stress, (c) Tresca stress, and (d) position of selected points (A, B, C, D).

Compared to spherical particles with same stresses on the surface, the difference is more than 3 times in a realistic Li_xC_6 particle. The simulation results of positive electrode particle 3 are shown in Figure 3.4, including (a) the lithium ion concentration,

(b) the von Mises stress (c) the tresca stress at selected point E ~ H at 110 s (SOC: 0.531) with 1 C intercalation. The lithium ion concentration on the surface area of the $LiCoO_2$ particle also depends on their geometric characteristics. The concentrations at those four points are 25830 mol/m^3 (E), 25850 mol/m^3 (F), 25800 mol/m^3 (G), and 25820 mol/m^3 (H). The von Mises stresses are 2.3 MPa (E), 0.25 MPa (F), 0.48 MPa (G), and 0.67 MPa (H). Point E is located on a sharp concave area and experienced the highest DIS during intercalation. The stress is almost 10 times higher than that at point F. The highly irregular shape of the particles accelerates the possibility of material failure. The dimpled point E of particle 3 might be a critical point that could start a physical crack.

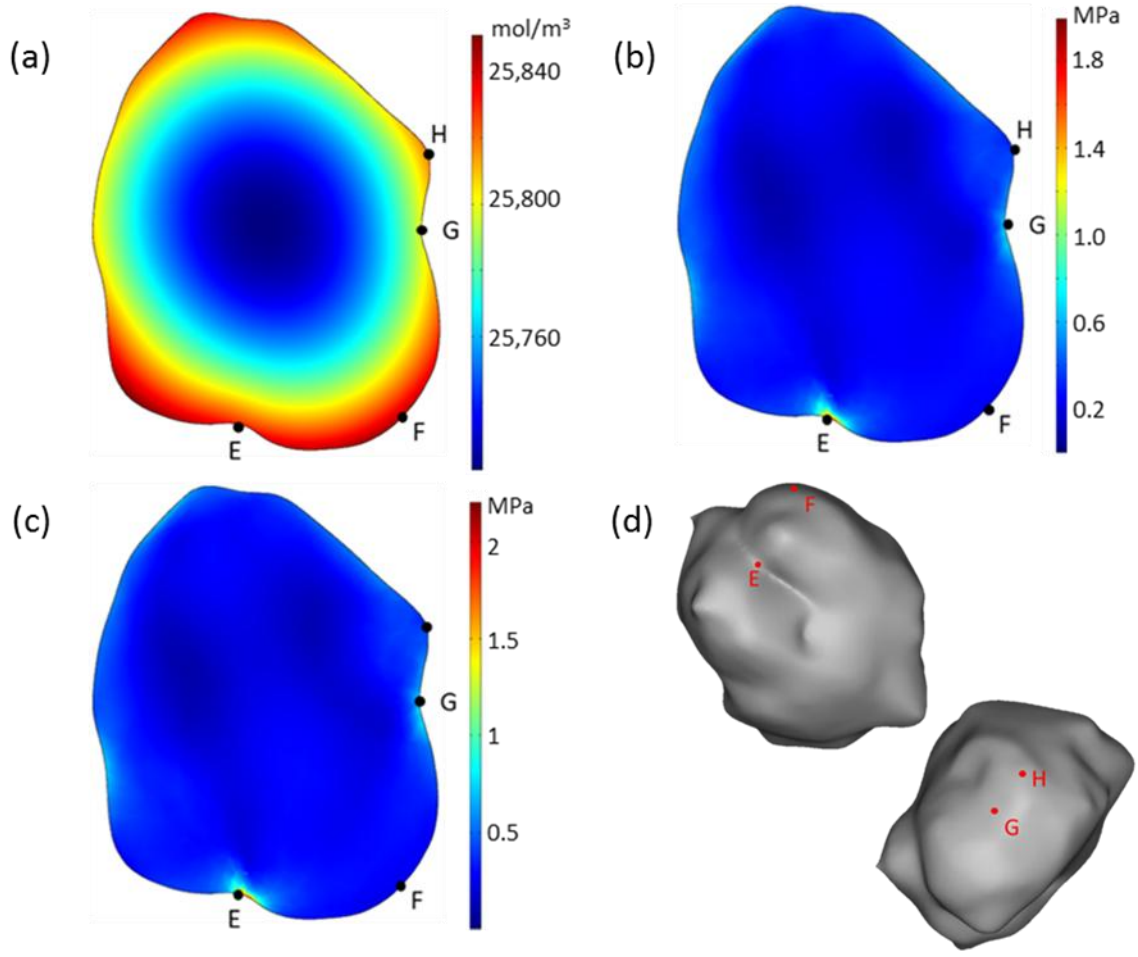

Figure 3.4 Simulation results of $LiCoO_2$ particle 3 at 110 s with 1 C intercalation condition, (a) concentration, (b) von Mises stress, (c) Tresca stress, and (d) position of selected point (E, F, G, H).

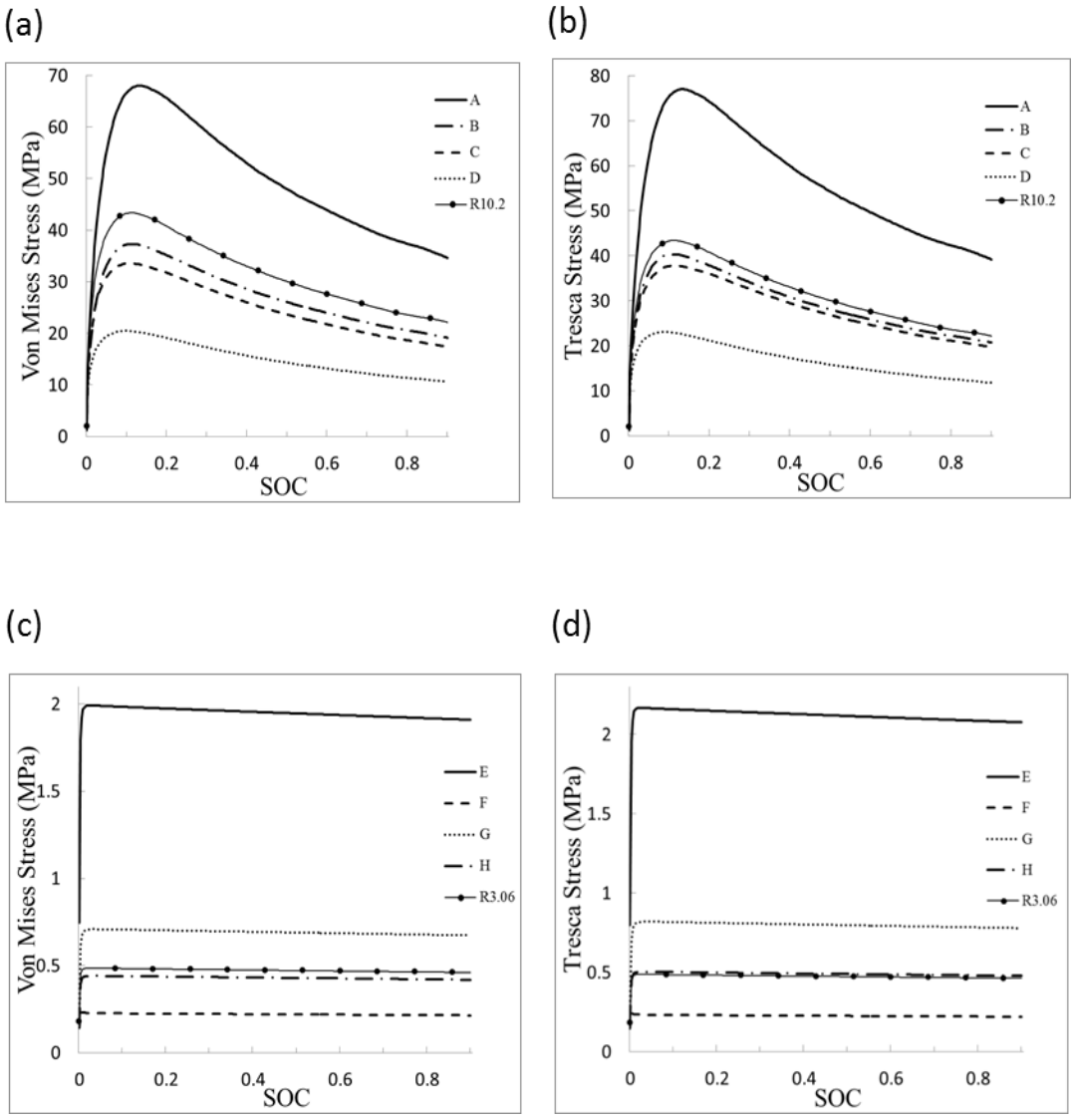

Figure 3.5 Diffusion-induced stress distribution at different state of charge with 1 C intercalation condition, (a) von Mises stress and (b) Tresca stress of LiC_6 particle 1 and its corresponding spherical particle R10.2, (c) von Mises stress and (d) Tresca stress of $LiCoO_2$ particle 3 and its corresponding spherical particle R3.06

Figure 3.5 shows the stress profiles of LiC_6 particle 1, $LiCoO_2$ particle 3, and their corresponding spherical shape particles during a 1 C intercalation process. As shown in Figure 3.5 (a), the highest von Mises stress of LiC_6 particle 1 is 68 MPa at point A. It is almost 1.5 times higher than the highest von Mises stress of the spherical particle with

10.2 μm radius. As shown in Figure 3.5 (c), point E has about 3.3 times higher stress compared to its corresponding spherical particle with 3.06 μm radius. The tresca stresses of the particles are slightly higher than their von Mises stresses, but they have similar patterns. The calculated stresses of the negative and positive active materials increase until they reached maximum values and then decrease during the rest of the intercalation process. This phenomenon can be explained by the interaction between lithium ion diffusion and diffusion induced hydrostatic stress. As shown in Equation 3.1, the DISes are determined by a lithium ion concentration gradient [29]. However, the diffusion induced hydrostatic stress can enhance the lithium ion diffusion in the active materials according to Equation 3.2 [27]. We also can see from Equation 3.2 that the hydrostatic stress term is always positive for both positive and negative materials. During an intercalation process, the hydrostatic stress gradient is negative if Ω (graphite) is positive. If Ω ($LiCoO_2$) is negative, the hydrostatic stress gradient is positive.

For both cases, the hydrostatic stress term is positive and it can enhance the diffusion process. For example, the maximum von Mises stress of the spherical graphite particle (R 10.2 μm) is 43.4 MPa at 400 s (SOC: 0.111) shown in Figure 3.5 (a). The enhanced lithium ion diffusion causes the von Mises stress to decrease to 22.1 MPa at 3240 s (SOC: 0.9) during continuous lithium ion intercalation. If the hydrostatic stress term is neglected in Equation 3.2, the von Mises stress retains the maximum value after it reaches the maximum stress. However, the stress decline caused by enhanced diffusion is lower in the LiCoO2 particles. Figure 3.5 (c) shows about a 5% von Mises stress decrease after the maximum stress. It is because the absolute value of partial molar volume of LiCoO2 is almost 9 times smaller than that of graphite.

Figure 3.6 (a) and (b) exhibit the maximum von Mises stress and maximum Tresca stress of various sized negative electrode particles at different C rates. P1 and P2 are reconstructed LiC6 particles, R6.9, R8.5, R10.2, R12 are spherical LiC_6 particles with radius 6.9, 8.5, 10.2, and 12 μm respectively, P3 and P4 are reconstructed $LiCoO_2$ particles, R1.56, R2.3, R3.06, R4 are spherical $LiCoO_2$ particles with radius 1.56, 2.3,

3.06, and 4 μm respectively. When the particle size is increased, the DIS is raised with an increased lithium ion flux on the due to the decreased surface to volume ratio. To avoid physical fracture, the critical size of the electrode materials was suggested at given charge and discharge rate requirements by Winter et al. [67].

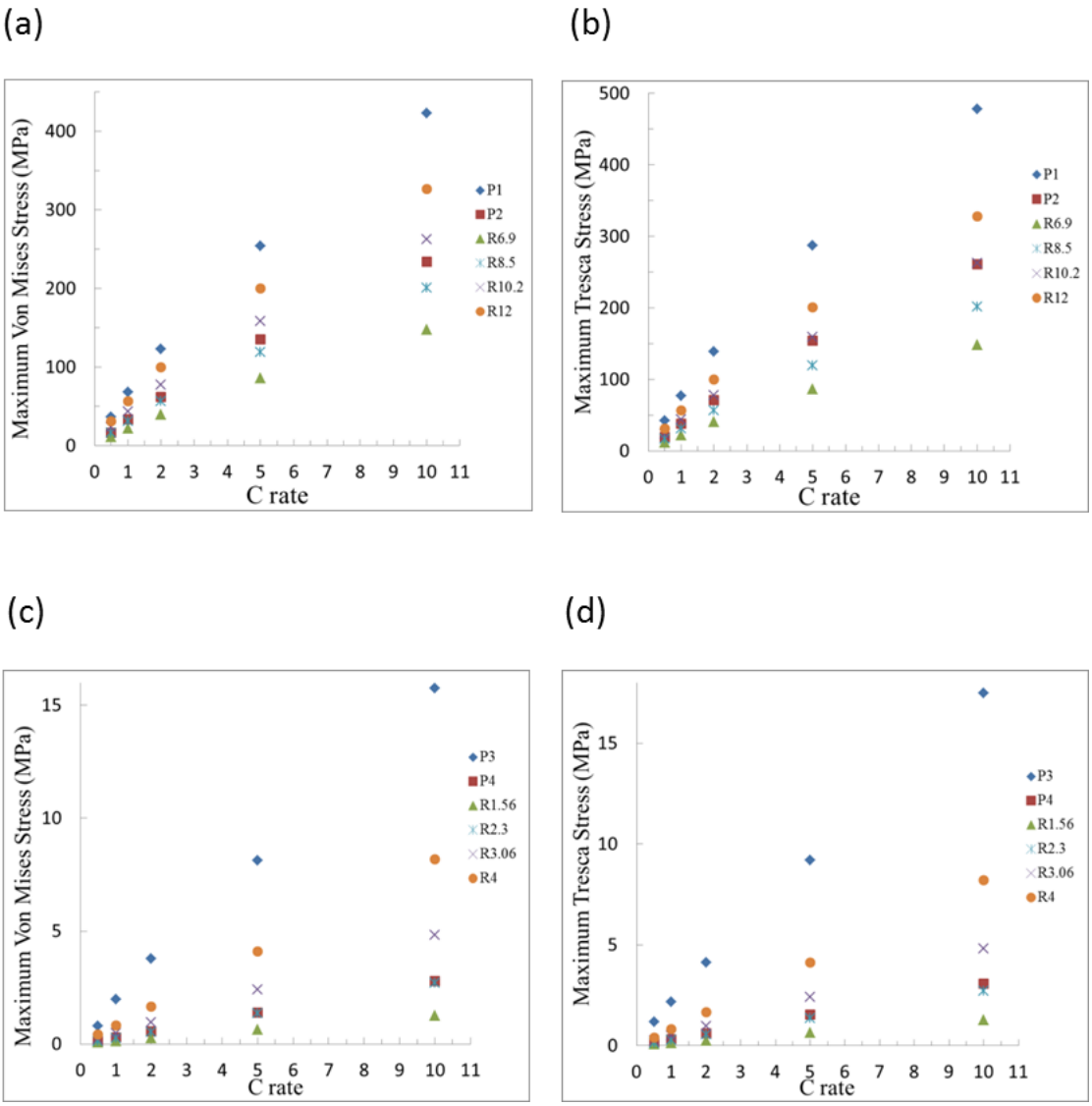

Figure 3.6 Maximum diffusion-induced stresses at various C rates intercalation conditions, (a) von Mises stress and (b) Tresca stress of LiC_6 particles, (c) von Mises stress and (d) Tresca stress of $LiCoO_2$ particles

However, the morphology of the active material particles also can cause high DIS. For example, graphite particle 2 with a 6.92 μm corresponding radius experiences 135 MPa maximum von Mises stress during a 5 C intercalation process, while the 8.5 μm radius spherical particle experiences 120 MPa. As shown in Figure 3.6 (c), the maximum von Mises stress in $LiCoO_2$ particle 3 is 3.4 times higher than its corresponding spherical particle (radius: 3.06 μm) at a 5 C intercalation process. Thus, the three dimensional geometry of active material particles should be considered as an important factor of material failure mechanism. The particles which experience stresses over the material's yield strength could initiate cracks and break into smaller particles eventually. If some of the broken particles lose the contact with electron conductive materials, the LIB will have capacity loss.

As shown in Figure 3.7, the DISes during an intercalation process are displayed with different C rates. P1 is the reconstructed LiC_6 particle, R10.2 is the corresponding spherical LiC_6 particles with 10.2 μm radius and the same volume as P1, P3 is the reconstructed $LiCoO_2$ particle, R3.06 is the corresponding spherical $LiCoO_2$ particle with 3.06 μm radius and the same volume as P3. The results show the relation between the state of charge and maximum DISes of the reconstructed electrode particles and their corresponding spherical particles. The diffusion-induced stresses of both negative and positive materials increase with an increasing lithium ion flux. The DIS tends to reach the maximum value at higher state of charge if higher C rates are used. For example, graphite particle 1 reaches the maximum von Mises stress at 0.133 SOC with a 1 C rate, while the maximum stress happens at 0.583 SOC with a 10 C rate. The maximum stress of $LiCoO_2$ particle 3 and the spherical shape particle also reaches the maximum value at higher SOC with an increasing C rate. At the same C rates, spherical particles reach the maximum DIS at a lower SOC than the irregular shape particles in both materials. However, the DISes of the negative particles increase slowly until they reached the maximum values, while the stresses of positive particles increase sharply. According to the analytic expressions of stress and strain energy under galvanostatic operation shown in reference [16], the SOC related to maximum DIS increases with increasing particle size, increasing

intercalation rate, and decreasing lithium diffusion coefficient. The high curvature concave areas on the surface of irregular particles can cause higher maximum DIS and it happens at higher SOC. Compared to graphite particles, $LiCoO_2$ particles have smaller size and higher diffusion coefficient, therefore the maximum DIS happens at much lower SOCs.

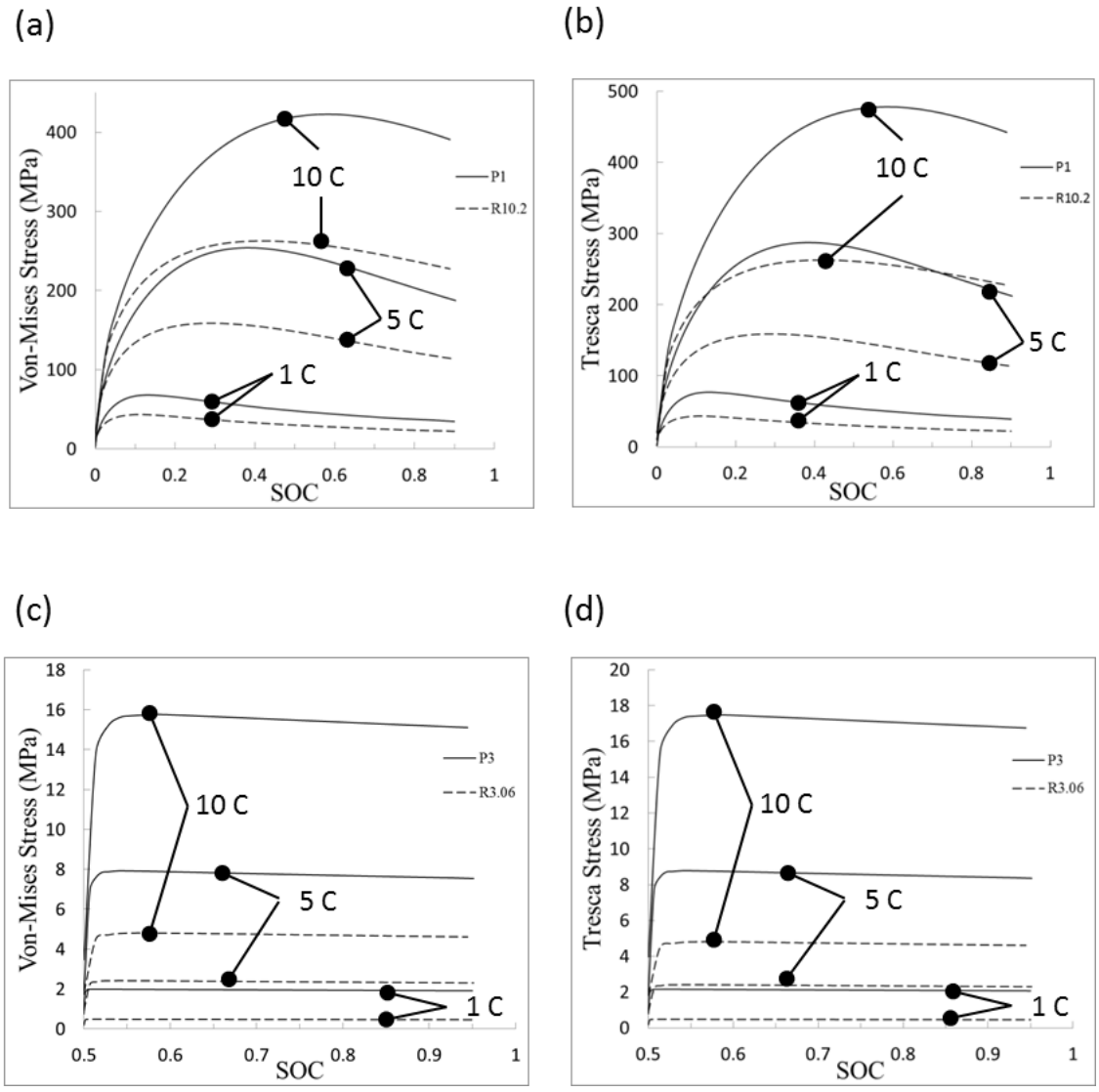

Figure 3.7 Diffusion induced stress distribution at different state of charge with various C rates intercalation conditions, (a) von Mises stress of LiC_6 particles, (b) Tresca stress of LiC_6 particles, (c) von Mises stress of $LiCoO_2$ particles, and (d) Tresca stress of $LiCoO_2$ particles

3.4. Conclusions

The diffusion-induced stresses in realistic active material particles were simulated for both negative and positive electrodes. The reconstructed particle structures were generated by micro/nano computerized tomography technology. The calculated stresses in reconstructed particles are 45 ~ 410% higher than the spherical shape particles which have same volume as the reconstructed particles. The results show that the diffusion-induced stress of reconstructed electrode particles depends on the local morphology of particles. In a sharp concave area of an electrode particle, the von Mises stress and Tresca stress are much greater than a smooth concave or convex area. It means that the mechanical failure could start at the sharp concave areas during lithium ion intercalation processes. The stresses also can be enhanced by other parameters, such as large particle size, large absolute value of partial molar volume, high Young's modulus of the material, and low lithium ion diffusion coefficient. These results suggest that certain tolerance should be taken to determine the design parameters when designing LIB electrodes because the irregular morphology of active material particles could cause much higher stresses than assumed spherical particles.

4. 3D SEMI-CELL SIMULATION

To incorporate intricate details, randomness, and other effects that occur in a real LIB, three dimensional simulation based on experimentally determined microstructure are desired. The purpose of this study is to describe a new method to study the effect of real microstructures on the performance of LIBs and guide the future LIB electrode design. In this work, a cathode ($LiCoO_2$) electrode of a commercial LIB was scanned to obtain the microstructure using x-ray nano-CT technology.

A three dimensional numerical framework was developed to simulate the galvanostatic discharge process based on the real microstructure. First, models for mass and charge conservation plus electrochemical kinetics are presented for homogeneous components of LIB electrode microstructure and finite volume method (FVM) [68-70] is employed to resolve the three dimensional coupled discharge formulations of an electrolyte-cathode semi-cell. Then the microstructure of cathode is reconstructed using nano-CT and the mesh generation of a semi-LIB microstructure is introduced.

The galvanostatic discharge process with different discharge rates under isothermal conditions is simulated using the presented models and FVM. Besides the discharge curves, the detailed electric and reaction fields including current density, potential, lithium ion concentration distribution, and the electrochemical reaction rate are reported.

4.1. Mathematical Model

4.1.1. Governing Equations

The governing equations used in this investigation include mass and charge conservation equations. In order to distinguish different materials, the subscripts of i = 1, 2, and 3 denote current collector, cathode active material particles and electrolyte. In the electric field of electrolyte, active material and current collector, no charge accumulation is assumed. In cathode active material particles and current collector, the transport of electrons is governed by Poisson's equation:

$$\nabla \cdot \mathbf{J} = \nabla \cdot \left(-\sigma_i \nabla \phi_i \right) = 0 \tag{4.1}$$

where $\mathbf{J}$ is current density vector, $i = 1,2$, σ_i is the conductivity of cathode active material particles or the current collector, and ϕ_i is electrostatic potential. While for electrolyte, the potential is governed by:

$$\nabla \cdot \mathbf{J} = \nabla \cdot \left[-k_3 \nabla \phi_3 + \frac{2k_3 RT}{Fc_3} \left(1 + \frac{\partial \ln f_3}{\partial \ln c_3} \right) \left(1 - t_+^0 \right) \nabla c_3 \right] = 0 \tag{4.2}$$

where k_3 is the conductivity of lithium ion in electrolyte, R is the universal gas constant, T is absolute temperature, F is Faraday's constant, t_+^0 is the transference number of lithium ion in electrolyte, c_3 is the molar concentration of lithium ion in electrolyte, f_3 is the mean molar activity coefficient of electrolyte and is assumed to be constant.

The mass conservation of lithium ion in cathode active material particles is governed by Fick's second law:

$$\frac{\partial c_2}{\partial t} = \nabla \cdot \left(D_2 \nabla c_2 \right) \tag{4.3}$$

where D_2 is the diffusivity of lithium ion in cathode active material particles, c_2 is the molar concentration of lithium ion in cathode active material particles.

For the transport of lithium ion in the electrolyte, the concentrated solution theory is applied. The convection effect is neglected and the species transportation equation is given by:

$$\frac{\partial c_3}{\partial t} = \nabla\left[D_3\left(1 - \frac{d\ln c_0}{d\ln c_3}\right)\nabla c_3 \right] - \frac{\mathbf{J}\cdot\nabla t_+^0}{z_+ \nu_+ F} \tag{4.4}$$

where c_0 and c_3 are the volumetric molar concentration of solvent and lithium ion concentration in electrolyte respectively, t_+^0 is the transference number of lithium ion in solution and is assumed to be constant in this study. So the last term on the right hand side of Equation 4.4 can be neglected. It is usually assumed that the solvent concentration is not a function of the lithium ion concentration, which implies that the second term in the bracket is 0.

In this study, side reaction is neglected. Lithium ion intercalation reaction across the interfaces of electrolyte and cathode material particles can be determined by the Butler-Volmer equation:

$$J^{\mathrm{Li}} = \frac{J}{F} = \frac{i_0}{F}\left\{ \exp\left(\frac{\alpha F}{RT}\eta\right) - \exp\left[-\frac{(1-\alpha)F}{RT}\eta\right]\right\} \tag{4.5}$$

where J^{Li} and J are the reaction flux of lithium ion and reaction current density respectively, i_0 is the exchange current density, η is surface overpotential, and α is a symmetry factor that represents the fraction of the applied potential promoting the cathodic reaction, α is 0.5 for the electrochemical reaction in LIBs. The exchange current density i_0 is given by:

$$i_0 = F k_0 (c_{3s})^{\alpha} (c_{\theta})^{\alpha} (c_{2s})^{1-\alpha} \tag{4.6}$$

where c_{3s} and c_{2s} are the lithium ion concentration in electrolyte and cathode active material particles at their interface respectively, c_{θ} is the difference between stoichiometric maximum concentration (solubility limit) and current concentration on the surface of the active material particles, $c_{\theta} = c_{\max} - c_{2s}$, and k_0 is a reaction rate constant. The overpotential η is defined as below:

$$\eta = \phi_2 - \phi_3 - U_{\mathrm{OCP}} \tag{4.7}$$

where ϕ_2 and ϕ_3 are the potential of cathode active material particles and electrolyte at the interface respectively , and U_{OCP} is the open circuit potential (OCP) at the interface.

4.1.2. Boundary Conditions

As the current flows from the cathode to the anode during discharge process, the zero potential $\phi = 0$ is imposed on the inflow boundary. The specified current density J is imposed on the outflow boundary:

$$\sigma \frac{\partial \phi}{\partial x_j} n_j = J \tag{4.8}$$

where $j = 1,2,3$, x_j is coordinate component and n_j is the unit vector normal to boundary surface. The other four boundary surfaces are set as the periodic boundary condition, which means no lithium ion flux and electronic flux cross these surfaces:

$$\sigma \frac{\partial \phi}{\partial x_j} n_j = 0,\ k \frac{\partial V}{\partial x_j} n_j = 0$$

The potential difference between the interface of active material particles and current collector due to imperfect bonding between them is modeled via contact resistance, R_C , as

$$\Delta \phi = I R_C \tag{4.9}$$

4.1.3. Finite Volume Method

The present finite volume method consists of time, space and equations discretization [68-70]. The time interval of interest is sub-divided into a number of subintervals δt and the space is discretized by a number of contiguous, non-overlapping control volumes (CVs) with the computational points at their centers. That means that the

values of potential and concentration are located at the centers of CVs. In this study, both potential and concentration are linearly distributed in the CVs space. The gradients of both values are estimated using the least square method. The FVM formulations for Equation 4.1 - 4.3 are given as follows:

$$\int_s \sigma_i \nabla \phi_i \cdot d\mathbf{s} = 0 \quad , \qquad i = 1,2 \tag{4.10}$$

$$\int_s \left[-k_3 \nabla \phi + \frac{2k_3 RT}{Fc_3} \left(1 + \frac{\partial \ln f}{\partial \ln c_3} \right) \left(1 - t_+^0 \right) \nabla c_3 \right] \cdot d\mathbf{s} = 0 \tag{4.11}$$

$$\int_V \frac{\partial c_i}{\partial t} dV = \int_s D_i \nabla c_i \cdot d\mathbf{s} \quad , \qquad i = 1,2,3 \tag{4.12}$$

4.2. Semi-Cell Model

4.2.1. 3D Geometry

In the present work, mesh was not generated via commercial software while a C++ code was developed to rebuild the microstructure of active material particles based on the scanned 2D images. The mesh of cuboid type is adopted to discretize the semi-cell and the material type of cuboid CV is determined by the grey level of the pixels which fill the cuboid CV. In the present work, the edge length of generated cuboid mesh for cathode active material particles is 384 nm. One volume of 15.36 × 15.36 × 40.32 μm was selected from the whole microstructure of cathode as the representative volume, of which the dimension of 40.32 μm is the thickness of the cathode. Once the microstructure of active material particles was obtained, the electrolyte occupies the open space and its microstructure can be reconstructed.

4.2.2. Mesh Generation

As a testing case, a semi-cell composed of electrolyte, active material particles and current collector is simulated in the present work. As shown in Figure 4.1, the

components are current collector, active material particles and electrolyte respectively from left to right. The mesh for the simulation includes 208000 CVs and 220211 vertices. The cathode electrode includes both active material particles and electrolyte. The electrolyte is in both the cathode electrode and the separator. Variant mesh densities in different regions are used to reduce number of mesh control volumes (CVs) thereby reducing the computation time. Because of the complex configuration of particles, the finest mesh is generated in the region of interaction between active material particles and electrolyte.

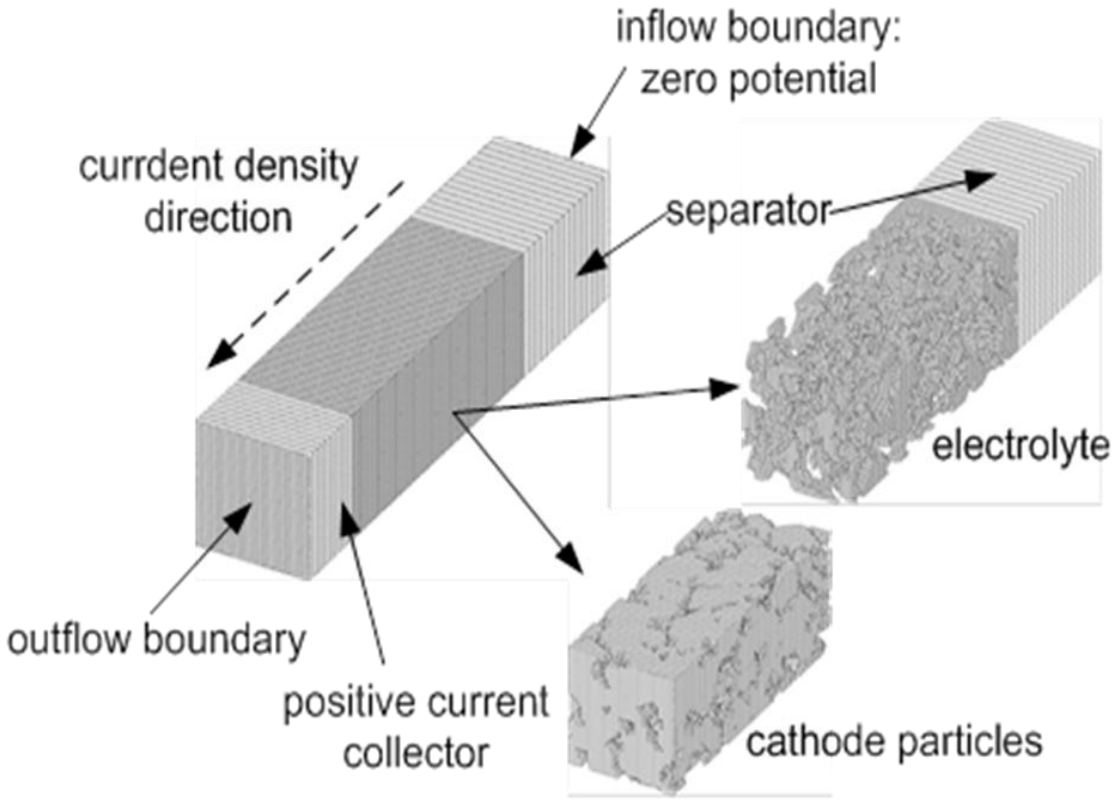

Figure 4.1 Illustration of a semi-cell and mesh generation for both electrode and electrolyte

4.2.3. Material Properties

The material properties in the above model are listed in Table 4.1. The OCP data are referred to the curve in reference [41] and [71] . The diffusivity of lithium ion in electrolyte and electrical conductivity of the electrolyte is referred in reference [13]:

$$\log D_3 = -4.43 - \frac{54}{T - 5\times10^3 c_3 - 229} - 0.22\times10^3 c_3$$

$$k_3 = c_l\left(-10.5 + 0.074T - 6.96\times10^{-5}T^2 + 668c_3 - 17.8c_3T + 0.028c_3T^2 + 4.94\times10^5 c_3^2 - 886c_3^2T\right)^2$$

where the subscript l denotes the electrolyte.

Table 4.1 List of material properties used in the model

	$LiCoO_2$	Electrolyte	Aluminum	Reference
σ (S/cm)	0.1		3.45×10^5	[11]
D (cm^2/s)	1×10^{-7}			[11]
t_+^0		0.2		[25]
R_C (Ωcm^2)	3.5			[25]
k_0 ($cm^{2.5}s^{-1}mol^{-0.5}$)		5×10^{-5}		[23]

The initial lithium ion concentration of electrolyte is set to be 1.0×10^{-6} mol/mm^3. The initial and maximum lithium ion concentration of $LiCoO_2$ particles are 2.38×10^{-5} mol/mm^3 and 4.99×10^{-5} mol/mm^3 respectively.

4.3. Results and Discussions

The response of a rechargeable lithium-ion battery is a combined result of all microstructures with complex geometry configuration. With the reconstructed microstructure based on real 3D images and the developed FVM program, the galvanostatic discharge process of a semi-cell with $LiCoO_2$ cathode was simulated. Discharge curves at different discharge rates are shown in Figure 4.2. The current density at different C rates was calculated based on the volume of the active materials in the representative microstructure and the energy density of $LiCoO_2$, 140 mA·h/g. The current density corresponding to 1C rate is about 1.8238×10^{-5} A/mm^2. The capacity is normalized by the total energy stored in the representative microstructure of $LiCoO_2$ cathode.

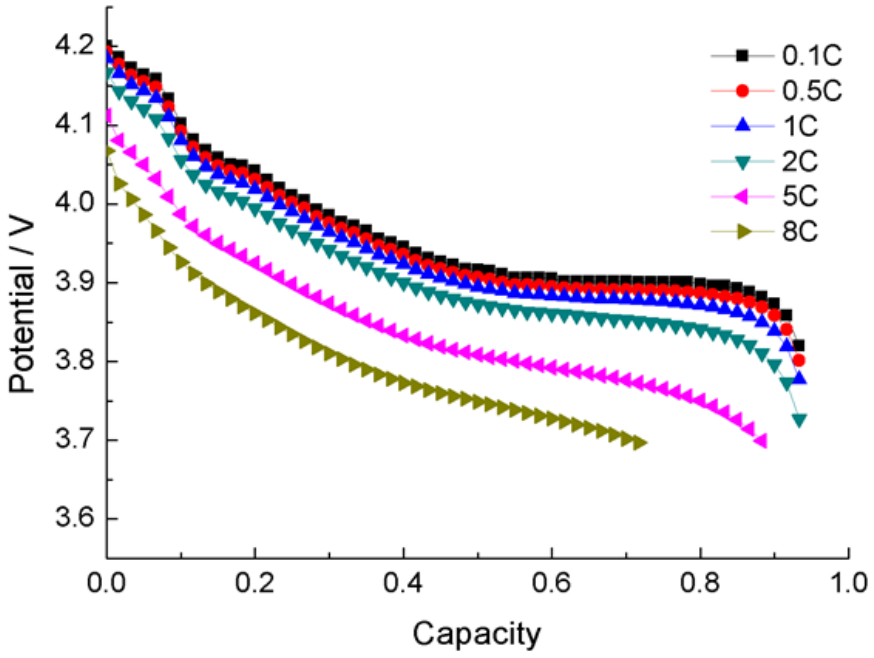

Figure 4.2 Normalized discharge curve of the representative volume from nano-CT images at different discharge rates

As shown in Figure 4.2, the high discharge rates cause more loss in the capacity of LIB. According to Equation 4.5, high reaction rate can cause high overpotential which will reduce the voltage of the cell. On the other hand, lithium ions accumulate on the surface due to the relatively low transport rate in the cathode particles when large

discharge rate is implemented. And the accumulated lithium ions on the particle surface can reduce the open circuit potential. Therefore, the overall capacity of the LIB is decreased at high discharge rates.

As expected, the 3D nature of this model can provide valuable insight into the spatial distribution of a variety of variable fields in the cathode electrode. When a discharge process with 1C rate is implemented, the concentration, potential, current density in cathode active material particles and electrolyte at time 4, 1600, and 3200 sec are shown in Figure 4.3 and 4.5 respectively. The reaction distribution at the interface between cathode active material particles and electrolyte at time 4, 1600, and 3200 sec is shown in Figure 4.6.

As shown in Figure 4.3 (a), the lithium ion concentration in the electrolyte reduces along the current direction. At the beginning of discharge process, lithium ion concentration is the same everywhere in the electrolyte. Because lithium ions need to diffuse through the complex ionic pathways to counteract the loss of lithium ions led by intercalation reactions in the region close to the current collector during discharge process, a lithium ion concentration gradient is developed as shown in Figure 4.3 (a). The gradient is expected to be higher if higher discharge rates are applied.

Figure 4.3 (b) shows that the voltage of electrolyte exhibits similar distribution as the lithium ion concentration, which can be explained by Equation 4.2. In the electrolyte, the current density generates joule heat which makes LIB temperature increase. Figure 4.3 (c) shows that the current density usually has a large value and will generate more joule heat in small ionic pathways.

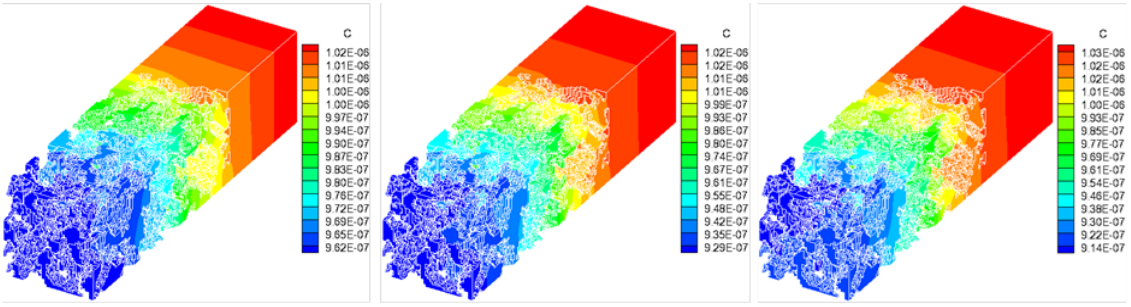

4 sec 1600 sec 3200 sec

(a) concentration (unit: mol / mm^3)

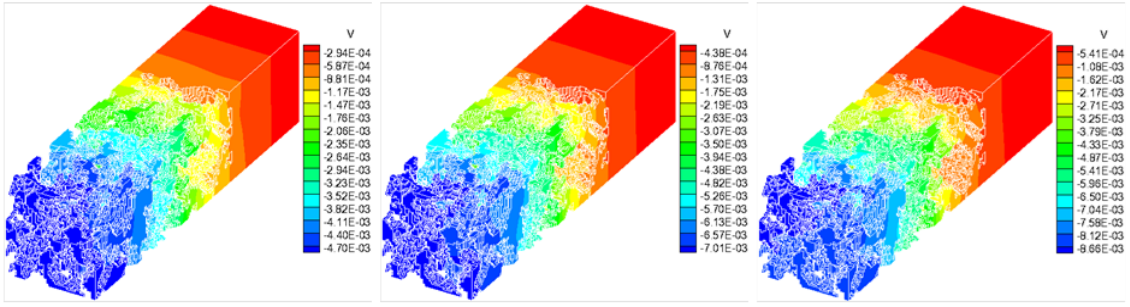

4s sec 1600 sec 3200 sec

(b) voltage (unit: V)

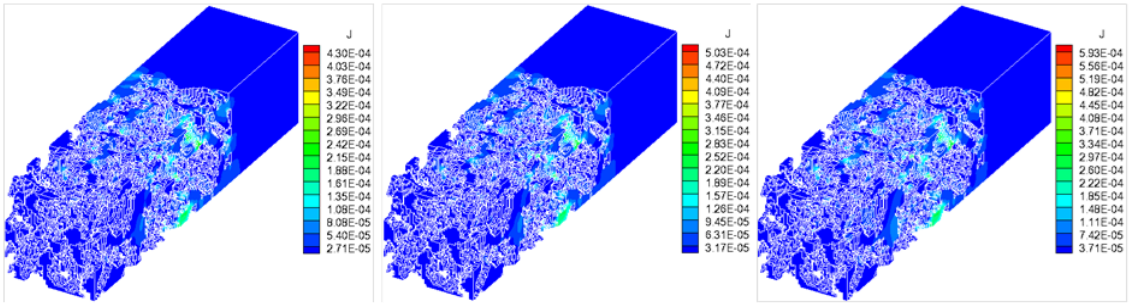

4 sec 1600 sec 3200 sec

(c) current density (unit: A / mm^2)

Figure 4.3 Distribution of physical variables in the electrolyte for the microstructure of electrolyte shown in Figure 4.1 at time 4, 1600 and 3200 sec respectively during 1 C discharge process

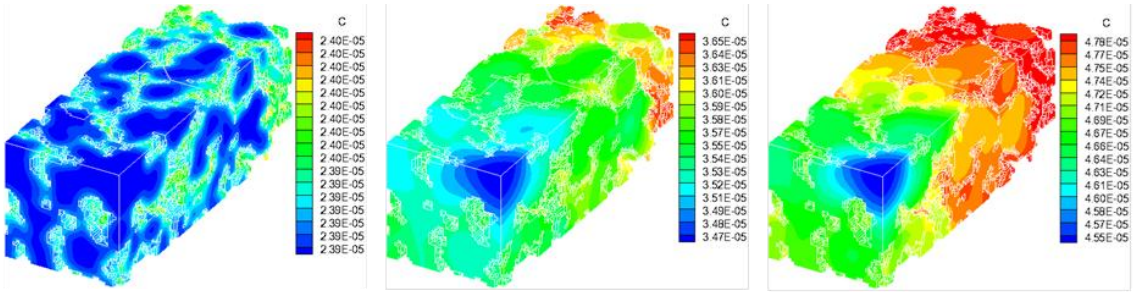

4 sec 1600 sec 3200 sec

(a) concentration (unit: mol / mm^3)

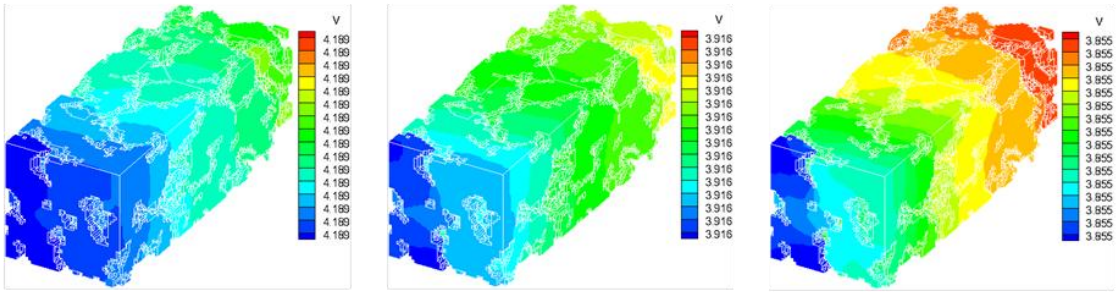

4 sec 1600 sec 3200 sec

(b) voltage (unit: V)

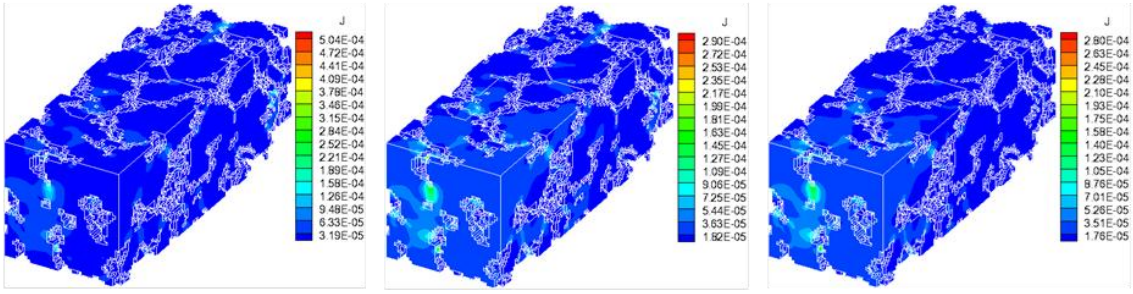

4 sec 1600 sec 3200 sec

(c) current density (unit: A / mm^2)

Figure 4.4 Distribution of physical variables in the cathode for the microstructure of cathode shown in Figure 4.1 at time 4, 1600 and 3200 sec respectively during 1 C discharge process

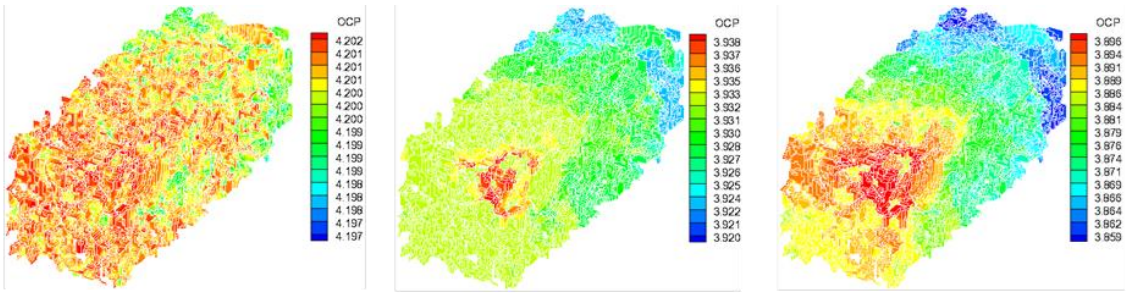

4 sec 1600 sec 3200 sec

(a) OCP (unit: V)

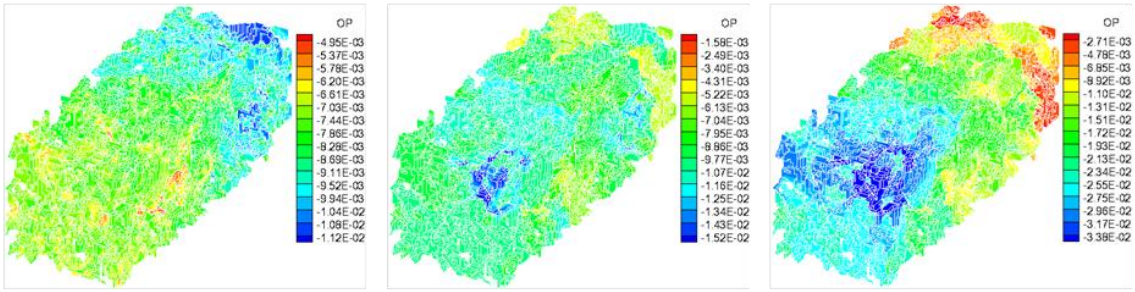

4s sec 1600 sec 3200 sec

(b) overpotential (unit: V)

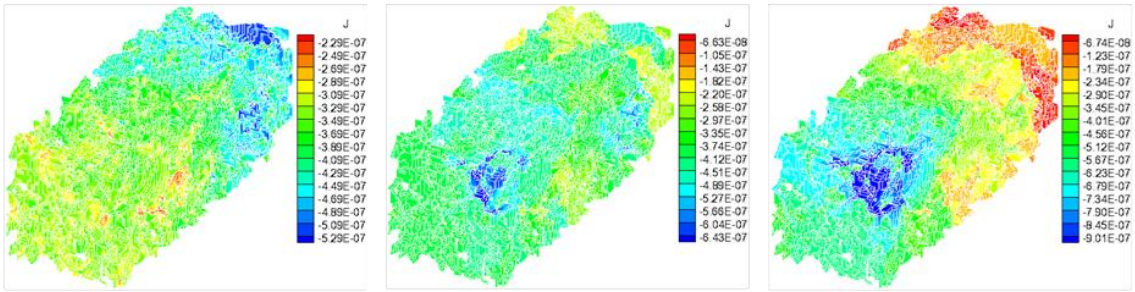

4 sec 1600 sec 3200 sec

(c) reaction rate (unit: A / mm^2)

Figure 4.5 Distribution of interfacial physical variables on the interface between cathode and electrolyte for the microstructure of cathode shown in Figure 4.1 at time 4, 1600 and 3200 sec respectively during 1 C discharge process

The lithium ion concentration distribution in the cathode active material particles is shown in Figure 4.4 (a). From these simulation results, we can find several features on the lithium ion concentration distribution. (1) The lithium ion concentration of small particles is usually higher than that of large particles. (2) The lithium ion concentration decreases along the current direction. (3) The variation of lithium ion concentration in the whole electrode is less than 10%.

Figure 4.4 (b) shows that the voltage variation in cathode active material particles is very small because of the relatively high electronic conductivity of the material. The voltage in the cathode particles can usually be reckoned as the same value. Based on the mathematical framework, the current density distribution in the cathode active materials was also simulated.

As shown in Figure 4.4 (c), the joint between cathode active material particles usually has smaller cross section area. The electrons flow through the section to neutralize the lithium ions at the surface of the particles. Then the current density at the joint is usually large and the electric current will generate higher joule heat at the joint than in other regions.

Because the microstructure of cathode active material particles is randomly distributed, the intercalation reaction on cathode active material particle surface is non-uniform and the spatial distribution of reaction rate is complicated. The OCP is assumed to be uniform in the cathode electrode at the beginning of discharge process. However, it becomes spatially different right after discharge process begins. As shown in Figure 4.5 (a), the distribution of overpotential and intercalation reaction rate are similar to the distribution of the electrolyte voltage at time 4 sec, while the OCP is almost the same everywhere. However, at time 1600 and 3200 sec, they exhibit similar distribution as the OCP when the variation of OCP increases. According to Equation 4.5, the intercalation reaction rate is determined by the overpotential and exchange current density if the temperature is assumed constant. The overpotential is related to the OCP and the voltage

of cathode active material particles and electrolyte at their interface, as shown in Equation 4.7.

The exchange current density is related to the lithium ion concentrations in cathode active material particles and electrolyte at their interface, as shown in Equation 4.6. When low discharge rates are applied, such as 1 C, the lithium ion concentration variation in both cathode active material particles and electrolyte is expected to be small because the diffusivity of lithium ion in electrolyte is 4 orders of magnitude higher than that in $LiCoO_2$.

This fact can be verified by the results shown in Figure 4.3 (a) and 4.4 (a), which show that the lithium ion concentration variation is less than 10%. In this case, the overpotential dominates the intercalation reaction rate. As shown in Figure 4.4 (b), the voltage variation in cathode active material particles is very small and it can usually be reckoned as the same value. The overpotential is determined by the OCP and the voltage in electrolyte. At the beginning of discharge process, the OCP is almost uniform and the voltage of electrolyte dominates the overpotential.

As shown in Figure 4.3 (b) and 4.5 (b), the overpotential distribution is similar to the electrolyte distribution and its absolute value decreases along the current direction. And the intercalation reaction rate shown in Figure 4.5 (c) also shows the similar distribution. According to reference [13], the OCP is only related to the state of charge on the surface of cathode active material particle. The OCP evolution should follow the same trend as lithium ion concentration. As the lithium ion concentration variation increases in cathode active material particles, the OCP starts to vary and distribute differently in the electrode. At about time 100 sec, the OCP start to dominate the overpotential, thereby determining the intercalation reaction rate.

The lithium ion concentration at the surface of cathode active material particles increases faster when the intercalation reaction rate is higher. However, the OCP will

decrease as the lithium ion concentration increases, which will decrease the intercalation reaction rate. Due to the negative feedback type relationship, the lithium ion concentration difference on the surface of cathode active material particles can not be very large during the discharge process.

Although the lithium ion concentration in smaller particles and the particles in the region close to the separator increases faster at the beginning of discharge process, the battery can regulate the lithium ion concentration distribution by the interaction of OCP and intercalation reaction rate. This can be verified by Figure 4.4 (a), which shows that the variation of lithium ion concentration in the whole electrode is less than 10% at different stage of discharge process. However, the variation of lithium ion concentration in both electrolyte and cathode active material particles is larger if higher discharge rates is applied, and so the variation of the overpotential is also larger.

As a result, the spatial distribution of intercalation rate at high discharge rates would be complicated, because the reaction rate is related to the complex microstructure of the electrode, the lithium ion concentration of both cathode active material particles and electrolyte at their interface, and the overpotential.

For the comparison of different discharge rates, the lithium ion concentration in cathode particles and electrolyte and the intercalation reaction rate with 5 C discharge rate at 600 sec are provided in Figure 4.6. The time of 600 sec with 5 C discharge rate is corresponding to 3000 sec with 1C discharge rate. When 5 C discharge rate is applied, the concentration variation in cathode active material particles is much larger compared to 1 C discharge (Figure 4.3 (a) and 4.4 (a)).

At high discharge rate, lithium ion transport through the ionic pathways are the limiting factor, which can cause low lithium ion concentration in the region close to the current collector in the electrolyte and the active material particles. As shown in Figure 4.6 (c), the reaction rate at the interface of cathode particles with 5C discharge rate is also

much higher than that with 1 C discharge rate. Because the intercalation reaction rate is determined by several factors, such as overpotential, lithium ion concentration on the surface of cathode particles, and the lithium ion concentration in the electrolyte, the reaction rate distribution is complicated and highly non-uniform.

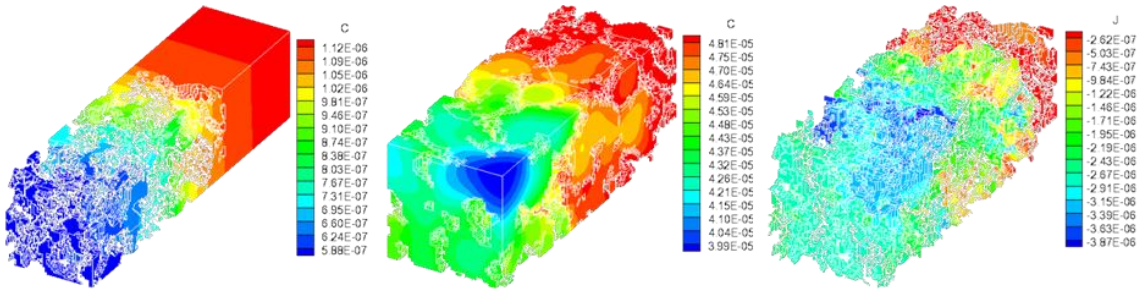

(a) concentration (unit: mol / mm^3)

(b) concentration (unit: mol / mm^3)

(c) reaction rate (unit: A / mm^2)

Figure 4.6 Variable distribution for the microstructure of cathode shown in Figure 4.1 at time 600 sec during 5 C discharge process

If a very large discharge rate is applied, the capacity of LIB can be decreased significantly due to the relatively slow lithium ion transport through the ionic pathways in the electrolyte. Because the lithium ions can not diffuse from the separator to the region close to the current collector for the intercalation reaction, the lithium ions will be consumed quickly and no intercalation reaction takes place in this region. In order to keep the same current density during galvanostatic discharge process, higher intercalation reaction rate will occur in the region close to the separator. More lithium ions will accumulate quickly at the surface of cathode particles near the separator, leading to quick decrease in OCP, which will cause large capacity loss.

The ionic transport resistance is affected by porosity, tortuosity, and thickness of the porous electrode. Although more cathode active materials can provide higher capacity, it also increases the thickness of cathode electrode leading to longer path for the lithium

ion diffusion or lower porosity. If the porosity of the cathode is very small, it will increase the resistance for lithium ions to diffuse into the region close to the current collector through the small channels between the cathode particles. Thus the capacity not only depends on the quantity of cathode active material, but also is confined by the diffusion resistance of lithium ions in the electrolyte especially at high discharge rates.

4.4. Conclusions

A three dimensional simulation framework of galvanostatic discharge of $LiCoO_2$ cathode based on x-ray nano-CT images and the corresponding FVM is presented in this paper. The corresponding software is developed to mesh the microstructure of cathode electrode and to simulate the discharge process with different discharge rates using FVM. The simulation results show that the response of a rechargeable LIB is a combined result of active material particles configuration, the porosity, the interactions among cathode particles, and the reaction between cathode particles and electrolyte. Based on the presented simulation results, the following conclusions may be deduced.

The randomly distributed microstructure of cathode particles leads to complicated and non-uniform distribution of variable fields, such as lithium ion concentration, overpotential, voltage, current density, and intercalation reaction rate in the cathode electrode. The voltage in the active material particles has very small variation due to the relatively high electronic conductivity of cathode materials. At the beginning of discharge process, electrolyte voltage dominates the overpotential and the intercalation reaction rate. When the lithium ion concentration variation increases on the surface of cathode particles, the open circuit potential (OCP) starts to dominate the overpotential and intercalation reaction rate. Large current density usually occurs at the joints between cathode particles. In the electrolyte, larger current density occurs at the smaller sections. More joule heat is generated in these regions. Higher discharge rates can cause more capacity loss. The variable fields distributions are more complicated due to the interaction among them. Because this study can give more valuable insight into the spatial distribution of a variety

of variable fields in the cathode electrode, it can be used to guide the design of LIB electrodes and improve the performance of LIBs.

5. CONCLUSIONS AND FUTURE WORK

5.1. Conclusions

The microstructures were constructed for graphite and lithium cobalt oxide electrodes of a commercial lithium ion battery. High resolution x-ray projected images were obtained by micro/nano-CT. The raw images successfully generated the 3D morphologies of the cathode and anode active materials.

Tortuosity of the microstructures has been calculated by a linear diffusion equation to characterize the 3D morphology. The obtained tortuosity and porosity results pointed out that the Bruggeman relationship is not sufficiently estimate the tortuosity by the porosity of electrodes. Because, the active materials are not homogeneous and regular shaped particles that are assumed in porous electrode thoery. The inhomogeneity of the materials causes higher tortuosity of the microstructures. Thus, the 3D morphology of electrodes might improve the results of computational simulations for lithium ion batteries.

The diffusion-induced stresses in realistic active material particles were simulated for both negative and positive electrodes. The calculated stresses in reconstructed particles are 45 ~ 410% higher than the spherical shape particles which have same volume as the reconstructed particles. The results show that the diffusion-induced stress of reconstructed electrode particles depends on the local morphology of particles. In a sharp concave area of an electrode particle, the von Mises stress and Tresca stress are much greater than a smooth concave or convex area. It means that the mechanical failure could start at the sharp concave areas during lithium ion intercalation processes.

A three dimensional simulation framework of galvanostatic discharge of $LiCoO_2$ cathode based on x-ray nano-CT images and the corresponding FVM is presented in this paper. The corresponding software is developed to mesh the microstructure of cathode electrode and to simulate the discharge process with different discharge rates using FVM. The simulation results show that the response of a rechargeable LIB is a combined result of active material particles configuration, the porosity, the interactions among cathode particles, and the reaction between cathode particles and electrolyte. Based on the presented simulation results, the following conclusions may be deduced.

Realistic geometries of electrodes have been applied to the lithium ion transport simulation, diffusion induced stress simulation, and semi-cell simulation. The results presented the complex 3D morphologies of the electrodes a crucial factor for numerical analysis of lithium ion batteries.

5.2. Future work

There is some more work that can be done in the future to improve the current mathematical model of LIBs as shown below.

- Lithium ion transport model should be simulated with anode current collector, reconstructed anode material, electrolyte, reconstructed cathode material, and cathode current collector.

- The diffusion induced model should be applied for reconstructed microstructures of the active materials to see the porosity change and study the delicate morphology.

- The electrode microstructures of cycled LIBs will be reconstructed to compare the morphology change of the active materials and capacity fade of the cell.

LIST OF REFERENCES

LIST OF REFERENCES

[1] J. Vetter, P. Novák, M. R. Wagner, C. Veit, K. C. Möller, J. O. Besenhard, M. Winter, M. Wohlfahrt-Mehrens, C. Vogler, and A. Hammouche, "Ageing mechanisms in lithium-ion batteries," *Journal of Power Sources*, vol. 147, pp. 269-281, 2005.

[2] E. Peled, "The Electrochemical Behavior of Alkali and Alkaline Earth Metals in Nonaqueous Battery Systems-The Solid Electrolyte Interphase Model," *Journal of The Electrochemical Society*, vol. 126, pp. 2047-2051, 1979.

[3] J. Li, E. Murphy, J. Winnick, and P. A. Kohl, "The effects of pulse charging on cycling characteristics of commercial lithium-ion batteries," *Journal of Power Sources*, vol. 102, pp. 302-309, 2001.

[4] S. S. Choi and H. S. Lim, "Factors that affect cycle-life and possible degradation mechanisms of a Li-ion cell based on $LiCoO_2$," *Journal of Power Sources*, vol. 111, pp. 130-136, 2002.

[5] J. Y. Song, H. H. Lee, Y. Y. Wang, and C. C. Wan, "Two- and three-electrode impedance spectroscopy of lithium-ion batteries," *Journal of Power Sources*, vol. 111, pp. 255-267, 2002.

[6] M. Broussely, S. Herreyre, P. Biensan, P. Kasztejna, K. Nechev, and R. J. Staniewicz, "Aging mechanism in Li ion cells and calendar life predictions," *Journal of Power Sources*, vol. 97–98, pp. 13-21, 2001.

[7] J. Christensen and J. Newman, "Stress generation and fracture in lithium insertion materials," *Journal of Solid State Electrochemistry*, vol. 10, pp. 293-319, 2006.

[8] J. W. Braithwaite, A. Gonzales, G. Nagasubramanian, S. J. Lucero, D. E. Peebles, J. A. Ohlhausen, and W. R. Cieslak, "Corrosion of Lithium-Ion Battery Current Collectors," *Journal of The Electrochemical Society*, vol. 146, pp. 448-456, 1999.

[9] J. N. Reimers and J. R. Dahn, "Electrochemical and In Situ X-Ray Diffraction Studies of Lithium Intercalation in Li_xCoO_2," *Journal of The Electrochemical Society*, vol. 139, pp. 2091-2097, 1992.

[10] R. Huggins and W. Nix, "Decrepitation model for capacity loss during cycling of alloys in rechargeable electrochemical systems," *Ionics*, vol. 6, pp. 57-63, 2000.

[11] G. G. Amatucci, J. M. Tarascon, and L. C. Klein, "Cobalt dissolution in $LiCoO_2$-based non-aqueous rechargeable batteries," *Solid State Ionics*, vol. 83, pp. 167-173, 1996.

[12] A. du Pasquier, A. Blyr, A. Cressent, C. Lenain, G. Amatucci, and J. M. Tarascon, "An update on the high temperature ageing mechanism in $LiMn_2O_4$-based Li-ion cells," *Journal of Power Sources*, vol. 81–82, pp. 54-59, 1999.

[13] X. Zhang, "Multiscale Modeling of Li-ion Cells: Mechanics, Heat Generation and Electrochemical Kinetics," Ph.D Dissertation, Mechanical Engineering, University of Michigan, 2009.

[14] J. Newman and W. Tiedemann, "Porous-electrode theory with battery applications," *AIChE Journal*, vol. 21, pp. 25-41, 1975.

[15] E. Markervich, G. Salitra, M. D. Levi, and D. Aurbach, "Capacity fading of lithiated graphite electrodes studied by a combination of electroanalytical methods, Raman spectroscopy and SEM," *Journal of Power Sources*, vol. 146, pp. 146-150, 2005.

[16] T. Ohzuku, H. Tomura, and K. Sawai, "Monitoring of Particle Fracture by Acoustic Emission during Charge and Discharge of Li/MnO_2 Cells," *Journal of The Electrochemical Society*, vol. 144, pp. 3496-3500, 1997.

[17] H. Gabrisch, R. Yazami, and B. Fultz, "Hexagonal to Cubic Spinel Transformation in Lithiated Cobalt Oxide," *Journal of The Electrochemical Society*, vol. 151, pp. A891-A897, 2004.

[18] H. Wang, Y.-I. Jang, B. Huang, D. R. Sadoway, and Y.-M. Chiang, "TEM Study of Electrochemical Cycling-Induced Damage and Disorder in $LiCoO_2$ Cathodes for Rechargeable Lithium Batteries," *Journal of The Electrochemical Society*, vol. 146, pp. 473-480, 1999.

[19] M. M. Thackeray, Y. Shao-Horn, A. J. Kahaian, K. D. Kepler, E. Skinner, J. T. Vaughey, and S. A. Hackney, "Structural Fatigue in Spinel Electrodes in High Voltage (4 V) $Li/Li_xMn_2O_2$ Cells," *Electrochemical and Solid-State Letters*, vol. 1, pp. 7-9, 1998.

[20] M. C. Tucker, J. A. Reimer, and E. J. Cairns, "A Li NMR Study of Capacity Fade in Metal-Substituted Lithium Manganese Oxide Spinels," *Journal of The Electrochemical Society*, vol. 149, pp. A574-A585, 2002.

[21] D. Wang, X. Wu, Z. Wang, and L. Chen, "Cracking causing cyclic instability of $LiFePO_4$ cathode material," *Journal of Power Sources*, vol. 140, pp. 125-128, 2005.

[22] H. Gabrisch, J. Wilcox, and M. M. Doeff, "TEM Study of Fracturing in Spherical and Plate-like $LiFePO_4$ Particles," *Electrochemical and Solid-State Letters*, vol. 11, pp. A25-A29, 2008.

[23] J. Christensen, "Modeling Diffusion-Induced Stress in Li-Ion Cells with Porous Electrodes," *Journal of The Electrochemical Society*, vol. 157, pp. A366-A380, 2010.

[24] J. Christensen and J. Newman, "A Mathematical Model of Stress Generation and Fracture in Lithium Manganese Oxide," *Journal of The Electrochemical Society*, vol. 153, pp. A1019-A1030, 2006.

[25] Y.-T. Cheng and M. W. Verbrugge, "Evolution of stress within a spherical insertion electrode particle under potentiostatic and galvanostatic operation," *Journal of Power Sources*, vol. 190, pp. 453-460, 2009.

[26] K. Zhao, M. Pharr, J. J. Vlassak, and Z. Suo, "Fracture of electrodes in lithium-ion batteries caused by fast charging," *Journal of Applied Physics*, vol. 108, p. 073517, 2010.

[27] X. Zhang, W. Shyy, and A. M. Sastry, "Numerical Simulation of Intercalation-Induced Stress in Li-Ion Battery Electrode Particles," *Journal of The Electrochemical Society*, vol. 154, pp. A910-A916, 2007.

[28] X. Zhang, A. M. Sastry, and W. Shyy, "Intercalation-Induced Stress and Heat Generation within Single Lithium-Ion Battery Cathode Particles," *Journal of The Electrochemical Society*, vol. 155, pp. A542-A552, 2008.

[29] J. Park, W. Lu, and A. M. Sastry, "Numerical Simulation of Stress Evolution in Lithium Manganese Dioxide Particles due to Coupled Phase Transition and Intercalation," *Journal of The Electrochemical Society*, vol. 158, pp. A201-A206, 2011.

[30] F. Yang, "Interaction between diffusion and chemical stresses," *Materials Science and Engineering*, A, vol. 409, pp. 153-159, 2005.

[31] M. Doyle, T. F. Fuller, and J. Newman, "Modeling of Galvanostatic Charge and Discharge of the Lithium Polymer Insertion Cell," *Journal of The Electrochemical Society*, vol. 140, pp. 1526-1533, 1993.

[32] M. Doyle and J. Newman, "The use of mathematical modeling in the design of lithium polymer battery systems," *Electrochimica Acta*, vol. 40, pp. 2191-2196, 1995.

[33] P. Arora, M. Doyle, A. S. Gozdz, R. E. White, and J. Newman, "Comparison between computer simulations and experimental data for high-rate discharges of plastic lithium-ion batteries," *Journal of Power Sources*, vol. 88, pp. 219-231, 2000.

[34] Q. Guo, V. R. Subramanian, J. W. Weidner, and R. E. White, "Estimation of Diffusion Coefficient of Lithium in Carbon Using AC Impedance Technique," *Journal of The Electrochemical Society*, vol. 149, pp. A307-A318, 2002.

[35] P. M. Gomadama, J. W. Weidner, R. A. Dougal, and R. E. White, "Mathematical modeling of lithium-ion and nickel battery systems," *Journal of Power Sources* vol. 110, p. 18, 2002.

[36] W. B. Gu, C. Y. Wang, J. W. Weidner, R. G. Jungst, and G. Nagasubramanianc, "Computational Fluid Dynamics Modeling of a Lithium/Thionyl Chloride Battery with Electrolyte Flow," *Journal of The Electrochemical Society*, vol. 147, pp. 427-434, 2000.

[37] S. Renganathan, G. Sikha, S. Santhanagopalan, and R. E. White, "Theoretical Analysis of Stresses in a Lithium Ion Cell," *Journal of The Electrochemical Society*, vol. 157, pp. A155-A163, 2010.

[38] Q. Zhang and R. E. White, "Moving Boundary Model for the Discharge of a $LiCoO_2$ Electrode," *Journal of The Electrochemical Society*, vol. 154, pp. A587-A596, 2007.

[39] W. Fang, O. J. Kwon, and C. Y. Wang, "Electrochemical-thermal modeling of automotive Li-ion batteries and experimental validation using a three-electrode cell," *International Journal of Energy Research*, vol. 34, pp. 107-115, 2010.

[40] C. Long and W. R. E., "Mathematical modeling of a lithium ion battery with thermal effects in COMSOL Inc. Multiphysics (MP) software," *Journal of Power Sources*, vol. 196, pp. 5985-5989, 2011.

[41] K. Kumaresan, G. Sikha, and R. E. White, "Thermal Model for a Li-Ion Cell," *Journal of The Electrochemical Society*, vol. 155, pp. A164-A171, 2008.

[42] K. E. Thomas and J. Newman, "Thermal Modeling of Porous Insertion Electrodes," *Journal of The Electrochemical Society*, vol. 150, p. A176, 2003.

[43] Y.-T. Cheng and M. W. Verbrugge, "Diffusion-Induced Stress, Interfacial Charge Transfer, and Criteria for Avoiding Crack Initiation of Electrode Particles," *Journal of The Electrochemical Society*, vol. 157, pp. A508-A516, 2010.

[44] R. Deshpande, Y.-T. Cheng, M. W. Verbrugge, and A. Timmons, "Diffusion Induced Stresses and Strain Energy in a Phase-Transforming Spherical Electrode Particle," *Journal of The Electrochemical Society*, vol. 158, p. A718, 2011.

[45] G. Ning and B. N. Popov, "Cycle Life Modeling of Lithium-Ion Batteries," *Journal of The Electrochemical Society*, vol. 151, p. A1584, 2004.

[46] P. Ramadass, B. Haran, P. M. Gomadam, R. White, and B. N. Popov, "Development of First Principles Capacity Fade Model for Li-Ion Cells," *Journal of The Electrochemical Society*, vol. 151, p. A196, 2004.

[47] X. Xiao, W. Wu, and X. Huang, "A multi-scale approach for the stress analysis of polymeric separators in a lithium-ion battery," *Journal of Power Sources*, vol. 195, pp. 7649-7660, 2010.

[48] R. E. Garcia, Y. M. Chiang, W. C. Carter, P. Limthongkul, and C. M. Bishop, "Microstructural Modeling and Design of Rechargeable Lithium-Ion Batteries," *Journal of The Electrochemical Society*, vol. 152, pp. A255-A263, 2005.

[49] T. F. Fuller, M. Doyle, and J. Newman, "Simulation and Optimization of the Dual Lithium Ion Insertion Cell," *Journal of The Electrochemical Society*, vol. 141, pp. 1-10, 1994.

[50] J. R. Wilson, W. Kobsiriphat, R. Mendoza, H.-Y. Chen, J. M. Hiller, D. J. Miller, K. Thornton, P. W. Voorhees, S. B. Adler, and S. A. Barnett, "Three-dimensional reconstruction of a solid-oxide fuel-cell anode," *Nat Mater*, vol. 5, pp. 541-544, 2006.

[51] J. R. Wilson, J. S. Cronin, A. T. Duong, S. Rukes, H.-Y. Chen, K. Thornton, D. R. Mumm, and S. Barnett, "Effect of composition of ($La_{0.8}Sr_{0.2}MnO_3$–Y_2O_3-stabilized ZrO_2) cathodes: Correlating three-dimensional microstructure and polarization resistance," *Journal of Power Sources*, vol. 195, pp. 1829-1840, 2010.

[52] J. R. Wilson, J. S. Cronin, S. A. Barnett, and S. J. Harris, "Measurement of three-dimensional microstructure in a $LiCoO_2$ positive electrode," *Journal of Power Sources*, vol. 196, pp. 3443-3447, 2011.

[53] J. John, R. Izzo, A. S. Joshi, K. N. Grew, W. K. S. Chiu, A. Tkachuk, S. H. Wang, and W. Yun, "Nondestructive Reconstruction and Analysis of SOFC Anodes Using X-ray Computed Tomography at Sub-50 nm Resolution," *Journal of The Electrochemical Society*, vol. 155, pp. B504-B508, 2008.

[54] P. R. Shearing, L. E. Howard, P. S. Jørgensen, N. P. Brandon, and S. J. Harris, "Characterization of the 3-dimensional microstructure of a graphite negative electrode from a Li-ion battery," *Electrochemistry Communications*, vol. 12, pp. 374-377, 2010.

[55] S. H. Lau, K. S. C. Wilson, G. Fernando, C. Hauyee, T. Andrei, F. Michael, and Y. Wenbing, "Non-invasive, multiscale 3D X-Ray characterization of porous functional composites and membranes, with resolution from MM to sub 50 NM," *Journal of Physics*: Conference Series, vol. 152, p. 012059, 2009.

[56] N. Epstein, "On tortuosity and the tortuosity factor in flow and diffusion through porous media," *Chemical Engineering Science*, vol. 44, pp. 777-779, 1989.

[57] H. W. Piekaar and L. A. Clarenburg, "Aerosol filters—the tortuosity factor in fibrous filters," *Chemical Engineering Science*, vol. 22, pp. 1817-1827, 1967.

[58] S. P. Rigby and L. F. Gladden, "NMR and fractal modelling studies of transport in porous media," *Chemical Engineering Science*, vol. 51, pp. 2263-2272, 1996.

[59] E. Bullitt, G. Gerig, S. M. Pizer, L. Weili, and S. R. Aylward, "Measuring tortuosity of the intracerebral vasculature from MRA images," Medical Imaging, *IEEE Transactions*, vol. 22, pp. 1163-1171, 2003.

[60] D. Gostovic, J. R. Smith, D. P. Kundinger, K. S. Jones, and E. D. Wachsman, "Three-Dimensional Reconstruction of Porous LSCF Cathodes," *Electrochemical and Solid-State Letters*, vol. 10, pp. B214-B217, 2007.

[61] T. Hutzenlaub, S. Thiele, R. Zengerle, and C. Ziegler, "Three-Dimensional Reconstruction of a $LiCoO_2$ Li-Ion Battery Cathode," *Electrochemical and Solid-State Letters*, vol. 15, pp. A33-A36, 2012.

[62] D. Kehrwald, P. R. Shearing, N. P. Brandon, P. K. Sinha, and S. J. Harris, "Local Tortuosity Inhomogeneities in a Lithium Battery Composite Electrode," *Journal of The Electrochemical Society*, vol. 158, pp. A1393-A1399, 2011.

[63] I. V. Thorat, D. E. Stephenson, N. A. Zacharias, K. Zaghib, J. N. Harb, and D. R. Wheeler, "Quantifying tortuosity in porous Li-ion battery materials," *Journal of Power Sources*, vol. 188, pp. 592-600, 2009.

[64] K. R. Kganyago and P. E. Ngoepe, "Structural and electronic properties of lithium intercalated graphite LiC_6," *Physical Review B*, vol. 68, p. 205111, 2003.

[65] R. H. Perry and D. W. Green, "Perry's Chemical Engineers' Handbook (7th Edition)," ed: McGraw-Hill, 1997.

[66] P. Ramadass, B. Haran, P. M. Gomadam, R. White, and B. N. Popov, "Development of First Principles Capacity Fade Model for Li-Ion Cells," *Journal of The Electrochemical Society*, vol. 151, pp. A196-A203, 2004.

[67] M. Winter, J. O. Besenhard, M. E. Spahr, and P. Novak, "Insertion Electrode Materials for Rechargeable Lithium Batteries," *Advanced Materials*, vol. 10, p. 725, 1998.

[68] I. Demirdzic and S. Muzaferija, "Numerical method for coupled fluid flow, heat transfer and stress analysis using unstructured moving meshes with cells of arbitrary topology," *Computer Methods in Applied Mechanics and Engineering*, vol. 125, pp. 235-255, 1995.

[69] H. Basic, I. Demirdzic, and S. Muzaferija, "Finite volume method for simulation of extrusion processes," *International Journal for Numerical Methods in Engineering*, vol. 62, pp. 475-494, 2005.

[70] I. Bijelonja, I. Demirdzic, and S. Muzaferija, "A finite volume method for incompressible linear elasticity," *Computer Methods in Applied Mechanics and Engineering*, vol. 195, pp. 6378-6390, 2006.

[71] M. Smith, R. E. García, and Q. C. Horn, "The Effect of Microstructure on the Galvanostatic Discharge of Graphite Anode Electrodes in LiCoO2-Based Rocking-Chair Rechargeable Batteries," *Journal of The Electrochemical Society*, vol. 156, pp. A896-A904, 2009.